A First Principles Investigation of Transitional Metal Doping in Lithium Battery Cathode Materials

by

Sarah H. Buta

S.B., Materials Science and Engineering, 1994
Massachusetts Institute of Technology

Submitted to the Department of Materials Science and Engineering
in partial fulfillment of the requirements for the degree of

Master of Science in Materials Science and Engineering
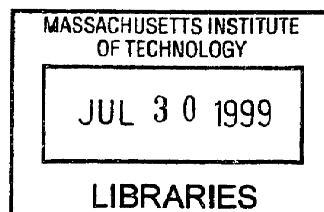
at the

MASSACHUSETTS INSTITUTE OF TECHNOLOGY

June 1999

Author ....
Department of Materials Science and Engineering
May 7, 1999

Certified by ....~~~~~~..
Gerbrand Ceder
Associate Professor of Materials Science
Thesis Supervisor

Accepted by ....
Linn W. Hobbs
John F. Elliott Professor of Materials
Chair, Departmental Committee on Graduate Students

A First Principles Investigation of Transitional Metal Doping in Lithium Battery Cathode Materials

by

Sarah H. Buta

Submitted to the Department of Materials Science and Engineering
on May 7, 1999 in partial fulfillment of the
requirements for the degree of
Master of Science in Materials Science and Engineering

Abstract

The goal of this work is to understand the properties of mixed-metal intercalation oxides. Using first-principles methods, the effect of doping on the mixing, energetic, and voltage properties as well as the phase diagrams of lithium transition-metal oxides for lithium battery cathode materials was investigated. The effect of doping on the phase separation tendencies of layered transition-metal oxides was examined and it was found that for normal processing temperatures, Al is miscible in layered transition metal oxides ($LiMO_2$) for five of the eight first-row transition metals studied. Temperature-composition phase diagrams for both $Li(Al,Co)O_2$ and $Li(Al,Cr)O_2$ were calculated. In these two systems, Al-doping is limited above 600°C by the formation of γ-$LiAlO_2$ and at very low temperatures owing to the existence of a miscibility gap. Reduced solubility is expected in the layered phase above 600°C for all oxides which have substantial solubility with $LiAlO_2$ due to the formation of γ-$LiAlO_2$.

The effect of transition-metal doping on the average voltage properties in Mn-based spinels was calculated and the large increase in average voltage found experimentally was reproduced. A detailed analysis on the layered structure $Li(Al,Co)O_2$ was performed, studying the energetics of different lithium sites and the effect of short-range clustering on the shape of the voltage curve. Though the *average* voltage is raised by Al substitution, the unexpected stability of sites with a few Al nearest neighbors leads to an initial decrease in voltage. For the Al-doped $LiCoO_2$ system, a step in the voltage curve is found only for micro-segregated materials. When the Al and Co ions are randomly distributed in a solid solution, the voltage curve shows a continuous, gradual slope.

The effect of oxygen defects in the $Li(Al,Co)O_2$ system was investigated. A model for the effect of oxygen vacancies on the free energy of doped layered oxides was created by combining an ideal gas approximation and first-principles energy defect calculations. The results qualitatively confirm experimental studies on oxygen release in lithium battery materials.

Thesis Supervisor: Gerbrand Ceder
Title: Associate Professor of Materials Science

To Mom and Dad,

for their constant encouragement.

Acknowledgements

Having the support of family and friends has greatly enriched my graduate experience. Their encouragement and belief in my abilities has supported me in throughout my education. With these people behind me, my life is a much richer and brighter place.

I want to thank my advisor, Gerd Ceder, for all the help and encouragement has given me over the past two years. He has allowed me to explore many opportunities and investigate ideas in my own way. His understanding and approach to research has almost made me want to continue on to earn a Ph.D.

My lab-mates and friends have truly made this whole graduate school experience worthwhile. Eric Wu was always ready to help keep me focused on the important things. Chris Marianetti and John Reed ensured that I was never bored. Anton Van der Ven never complained when I asked him to explain a concept to me again and again. Axel van de Walle, S. K. Mishra, and Takeshi Takahashi provided valuable insights into our research projects. Kadri Aydinol, Carles Comas, and Adrian Kohan all were glad to help a naive first year graduate student get on top of things in lab. Dane Morgan spent way too many hours working with me on thermodynamics issues. I truly appreciate the help he gave me in putting together this thesis.

Outside of lab, there are four people who help me understand that while research and science are both meaningful, we all have other aspects of our life as well. Sossity Sheets, Mindy Tupper, Surekha Vajjhala, and Suzanne Wallace were great inspirations to me as wonderful women and friends. They were truly supportive of me through those first-year classes and the general exam.

My parents and family have always supported me and my interest in science and math. Though I was the only female in some of my classes, I never felt intimidated or unsure of my own abilities. Their unconditional love and encouragement of my sometimes zany approach to life has allowed to come as far as I have. My father especially has taught me that I can reach as far as I dream to go. Thank you.

But of course, I owe this all to the most wonderful and supportive husband and friend I could ever imagine. Sanjay always shows the most incredible faith in me, believing I can do anything. Luckily some of that has worn off on me, and I now take chances to go places I would not have gone without him.

Contents

Chapter 1

Introduction

There is a great deal of scientific and technological interest in developing improved rechargeable battery systems for use in portable electronic devices, backup power systems, and electric vehicles. Experimental studies have focused on the development of all aspects of the battery: new or improved anodes, electrolytes, and cathodes. Requirements for improved batteries include cyclability and reversibility, high energy and power density, safety, limited environmental impact, and low cost.

Rechargeable batteries using lithium intercalation compounds as the cathode and lithium metal as the anode have been extensively studied during the past decade. Lithium transition-metal oxides have attracted attention as cathode materials due to their high voltage with respect to metallic Li, relatively fast kinetics, high energy density, and low cost. These oxides have a large stability region with respect to lithium content. For some of these oxides, for example Li_xCoO_2, the ratio of lithium to metal ions can vary from 0 to 1 without significant change in the material's structure. The most suitable types of these oxide materials are insertion compounds, $Li_xM_yO_z$, with an open structure capable of accepting and releasing x number of lithium ions per mole of M_yO_z. A lithium anode in conjunction with an intercalation cathode and electrolyte produces cells operating with a reversible reaction, referred to as a lithium insertion or lithium intercalation process. This process essentially consists of inserting and extracting mobile lithium ions and compensating electrons into a rigid host structure. The Li^+ ions reversibly enter the host structure and the compensating electrons induce reversible changes in the oxidation state of M. (See Figure 1.1)

The equilibrium voltage difference between the two electrodes, also referred to as the
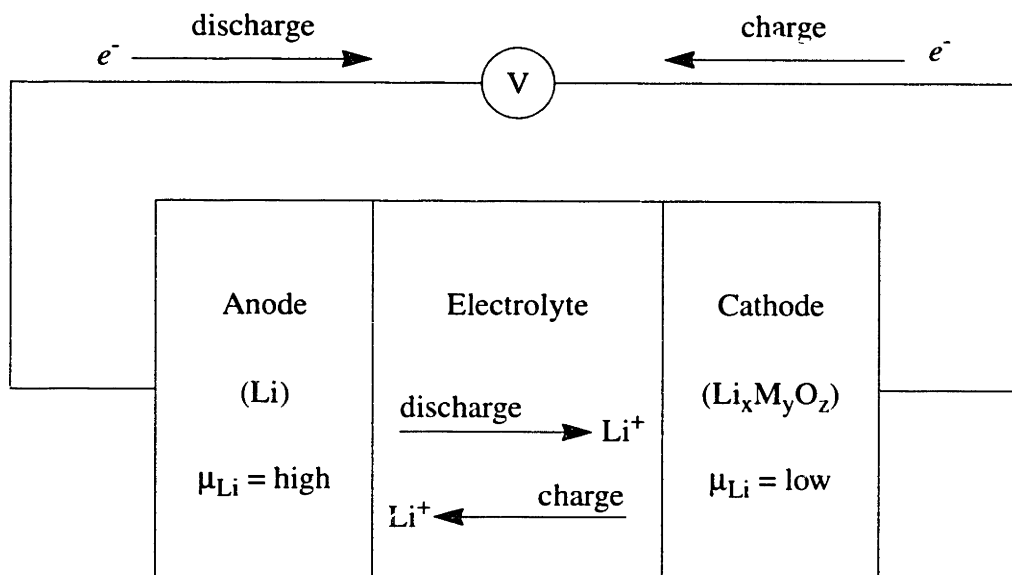
Figure 1.1:   Schematic of a rechargeable lithium battery. Li ions are removed from the cathode during charge and intercalate into the cathode when discharging.

open circuit voltage (OCV), depends on the difference in the lithium chemical potential between the anode and the cathode. For a battery, a large difference in chemical potential between the two electrodes is desirable as this leads to a high OCV. Two successful materials currently used commercially as cathodes are $LiCoO_2$ and $LiMn_2O_4$. These lithium intercalation compounds have a high OCV and provide high energy and power density. They are not without problems, however. $LiCoO_2$ is quite costly and toxic to the environment while $LiMn_2O_4$ shows cycling problems and a lower potential.

To overcome cycling problems and to increase the OCV in these rechargeable lithium batteries, one approach is to substitute different metals in the pure metal oxides in both the layered $(Li_xM_yM'_{1-y}O_2)$ and spinel crystal structures $(Li_xM_yM'_{2-y}O_4)$. Small amounts of transition-metal doping in manganese spinels $(LiM_yMn_{2-y}O_4)$ have been shown to improve cycling performance with little capacity loss [1, 2, 3, 4, 5, 6, 7, 8]. Aluminum, though not a transition metal, improves performance in these manganese lithium battery materials as well. Al substitution of the transition-metal cation has been shown theoretically and experimentally to increase cell voltage [9]. Doping with Al has been shown experimentally to improve the cycle-life and high-temperature stability of Mn-based insertion oxides [10] as well as $LiNiO_2$

[11]. Additional advantages of Al are that it is light, non-toxic, and inexpensive.

Experiments to discover the effectiveness of new cathode materials require an immense amount of time and labor for synthesis, characterization, and cycling. By combining first-principles quantum chemistry models with the rapid increase in computer power over the last decade, it is possible to accurately calculate the energies of solids. We are attempting to use these tools to predict microscopic and macroscopic behavior to discover favorable new cathode materials, thereby avoiding needless experimentation and focusing our efforts solely on the materials that promise success. In this work, we computationally study the effect of doping on the miscibility, energetic, and voltage properties of lithium transition-metal oxides for use as lithium battery cathode materials.

In Chapter 2, we describe the methodology used to perform the computations. Throughout this work, we use *ab initio* pseudopotential methods to compute the total energies of various structures. Using the energies of a small number of compounds, we parameterize the energy of the solid with a lattice model, enabling us to calculate the energy of any arrangement of atoms within the lattice at any composition. Finally, the energy of the entire system is used in conjunction with statistical mechanics to determine thermodynamic properties from which voltage curves and phase diagrams can be derived.

In Chapter 3, we study the miscibility of Al in eight first-row transition metal oxides, $LiAl_{1-y}M_yO_2$, and find that five of the eight first-row transition metals studied, (Cr, Co, Ni, Cu, and Fe) can be doped with Al if high enough processing temperatures are used. The temperature-composition phase diagrams are calculated for both $LiAl_{1-y}Co_yO_2$ and $LiAl_{1-y}Cr_yO_2$. A low temperature miscibility gap is found for the $Li(Al,Co)O_2$ system. Al-doping is limited above 600°C by the formation of γ-$LiAlO_2$. For all oxides which have substantial solubility with $LiAlO_2$ in the layered phase, we expect reduced solubility above 600°C due to the formation of γ-$LiAlO_2$.

In Chapter 4, we study the effect of doping on the intercalation voltage properties in both spinel and layered lithium transition metal oxides. We investigate the effect of transition-metal doping on the average voltage properties in Mn-based spinels, $LiM_yMn_{2-y}O_4$ (M = Cr, Fe, Co, Ni and Cu), and a detailed analysis is performed on the layered structure $Li(Al,Co)O_2$. The

energetics of different lithium sites are studied and we find that Li sites with one or two Al nearest neighbors are less stable than those surrounded entirely by Co. This unexpected stability leads to an initial decrease in voltage upon charging with respect to the voltage of pure $LiCoO_2$, though the *average* voltage is raised by Al substitution. We also examine the effect of short-range cation clustering on the voltage curve for Al-doped $LiCoO_2$. We find that micro segregation of Co and Al causes a step in the voltages curves, but in a solid solution the voltage curve shows no step.

In Chapter 5, the effect of oxygen vacancies in the $Li(Al,Co)O_2$ system is investigated. Combining an ideal gas approximation with first-principles calculations for the defect energy of an oxygen vacancy, we derive a model for determining the change in free energy for doped oxides as a function of temperature and pressure. Our preliminary results show that any effects due to the inclusion of oxygen vacancies on the phase diagram for $Li(Al,Co)O_2$ only occur at high temperatures, above 2000°C. The results also show that oxygen defects affect $LiCoO_2$ much more strongly than $LiAlO_2$, and that delithiated CoO_2 shows a greater tendency toward releasing oxygen.

In Chapter 6, we summarize our results and offer suggestions for further research.

Chapter 2

Methodology

First-principles modeling refers to the use of quantum mechanics to determine the structure and properties of materials. In this chapter, we describe the use of first-principles methods to obtain information on the phase separation tendencies, energetics, and voltage properties in lithium metal oxides for rechargeable lithium batteries.

All of the work done in this study begins with first-principles energy calculations at 0 K to determine the total energy of various structures. By comparing energy values of different compounds, we can predict the mixing tendencies and average voltages for a range of lithium compositions. In order to calculate phase diagrams and detailed intercalation curves, a free energy model is constructed to calculate behavior at non-zero temperatures. A cluster-expansion based on the 0 K total energies is built to parameterize the energy as a function of ionic arrangement. The interactions obtained from the cluster expansion are then used in conjunction with Monte Carlo simulations, a standard statistical mechanics method, to calculate the free energies of the system.

2.1   First-Principles Energy Calculations

The equations that govern interactions between the electrons and the nuclei of the solid have been well-known for many decades, but finding their exact solution for a complex solid is beyond the limits of current computing power. However, using a series of approximations, the electronic structure and thus the total energy of most materials can be calculated quite accurately.

There is a wide range of first-principles methods used to determine the behavior of materials. Materials have different types of bonding interactions and therefore some approximations are better suited than others for each system of interest [12]. The modern quantum-mechanical techniques to compute total energies used here are based on the density-functional theory [13]. In principle, this framework allows us to exactly map the problem of solving the Schrödinger equation for many interacting electrons onto that of a single electron moving in a non-local potential. This potential is not known exactly and several approximations can be used to represent it. One of the most commonly used expressions is a local representation of the effective potential called the local-density approximation (LDA) [14]. In this work we solve the Schrödinger equation within the LDA by using the pseudopotential method. Although originally developed for metals and semiconductors, the accuracy of the pseudopotential method is now well established for use in oxides [15, 16, 17, 18, 19, 20]. It has been found previously that the total energies in these oxide systems can be well predicted with pseudopotential approximations. [15, 21, 22].

The Vienna Ab initio Software Package (VASP) pseudopotential program [23, 24] used here solves the Kohn-Sham equations within LDA using ultra-soft pseudopotentials [25, 26]. All crystallographic degrees of freedom are optimized such that the minimum ground state energy is obtained. The VASP program implements the Ceperley and Alder [27] exchange and functional correlation as parameterized by Perdew and Zunger [28] in the energy calculations. The method of Monkhorst and Pack [29] is used to parameterize the k-space sampling. During relaxation calculations, the ionic positions and the lattice parameters of each structure are relaxed with the conjugate gradient method using forces and stresses. Also during relaxation, the method of Methfessel and Paxton [30] is used to treat the partial occupancy of the Fermi level. The energies of the optimized geometries are recalculated after each relaxation run, holding the atomic positions and the volume static. In these static runs, k-space integrations are performed using the linear tetrahedron method including corrections according to Blöchl et al. [31]. In the total energy calculations for the Li(Al,Co)O_2 system, and for most of the average voltage calculations in the doped spinel structures (Chapter 4), a plane wave basis set cutoff energy of 600 eV was used. For the most of the remainder of the first-principles energy

calculations, the cutoff energy was set to 400 eV, used in conjunction with the ultra-soft oxygen pseudopotential. This lower value was found to be sufficient to ensure a convergence.

2.2   Voltages and Gibbs Free Energy

On the cathode side of a rechargeable lithium battery, lithium is stored by insertion into the crystal structure of the host material. Upon charging and discharging, lithium ions leave and enter the host structure, respectively. The equilibrium potential of an electrochemical cell, which is the open circuit voltage, depends on the chemical potential difference for lithium between the anode and cathode materials [15, 22, 32, 33]:

$$V(x) = - \frac{\mu_{Li}^{cathode}(x) - \mu_{Li}^{anode}}{zF} \qquad 2.1$$

where z is the number of electrons transferred, in this case $z = 1$, and F is the Faraday constant. For simplicity we use the chemical potential for metallic lithium as the anode potential and the potentials are all referenced against pure lithium. With this definition of zero potential, and expressing μ_{Li} in electron volts (so $F = 1$), Equation 2.1 becomes:

$$V(x) = -\mu_{Li}^{cathode}(x) \qquad 2.2$$

With Equation 2.2, the voltage can easily be determined from the chemical potential of lithium in the cathode, and the relation between voltage measurements and thermodynamics is clear. Information about the intercalation profile can now be found from knowledge of the Gibbs free energy of lithium dissolution into the host. The lithium chemical potential is the partial derivative of the Gibbs free energy of lithium in the host, with respect to the number Li ions:

$$\mu_{Li} \equiv \left(\frac{\partial G_{host}}{\partial N_{Li}} \right)_{T, P, N_{host}} \qquad 2.3$$

where G_{host} is the free energy, T is temperature, P is pressure, and N_{host} is the number of host

molecules. In this case, N_{host} is constant and so N_{Li} is linear in x_{Li}, the concentration of Li ($N_{Li} = x_{Li} \cdot N_{host}$). Equating the partial derivative of the free energy with respect N_{Li} to the partial derivative of the molar free energy with respect to the concentration of Li allows us to determine the chemical potential as a function of the derivative of the molar free energy, $\underline{G}_{host}$:

$$\mu_{Li} = \left(\frac{\partial \underline{G}_{host}}{\partial x_{Li}}\right)_{T, P, N_{host}} \qquad 2.4$$

In addition, the free energy behavior can be found from the chemical potential, which allows the calculation of phase diagrams:

$$\underline{G}_{host}(x_{Li}) = \underline{G}_{host}(x_o) + \int_{x_o}^{x_{Li}} \mu_{Li}dx \qquad 2.5$$

where x_o is any reference concentration where the free energy is known.

2.3   Cluster Expansion

For intercalation compounds with delocalized valence electrons, the dominant contribution to the energy of mixing is from the configurational degrees of freedom associated with distributing ions within the host. Lattice models work well to describe the dependence of the energy of a crystal as a function of the ion arrangement. The energy expressions of simple lattice models are actually simplifications of a rigorous formalism called the cluster expansion method [34, 35, 36, 37], which is obtained by systematically coarse graining the non-configurational degrees of freedom of the system [38]. It is the ability to express the dependence of the crystal energy on configuration with the cluster expansion method that has made it possible to perform first-principles calculations of intercalation curves and temperature-composition phase diagrams [33].

The formalism to calculate the free energy of systems with binary disorder from first principles is well known [35, 38, 39] and consists of parameterizing the effect of ionic configuration on the energy with a lattice model. This method has been successfully applied to

the Li-intercalation behavior in layered $LiCoO_2$ [40] and spinel $LiCo_2O_4$ [41]. We can also extend this model to systems with binary disorder on two sublattices as is the case in $Li_x(Al,Co)O_2$ [42].

Within the Li-vacancy sublattice, the occupation variable σ_i is assigned, having the value +1 if site i is occupied and -1 if vacant. The dependence of the structure's energy on the configuration of Li-vacancy can then be expanded in terms of polynomials of these discrete occupation variables [34]:

$$E = V_o + \sum_\alpha V_\alpha \phi_\alpha \qquad 2.6$$

where V_o is the empty cluster and

$$\phi_\alpha = \prod_{i \in \alpha} \sigma_i \qquad 2.7$$

The polynomial basis functions, ϕ_α, correspond to products of occupation variables belonging to different clusters, α, of lattice sites such as pairs, triplets, etc. The sum in Equation 2.6 includes polynomials corresponding to all possible clusters on each Li plane and between different Li planes in the sublattice. In practice the constant expansion coefficients, V_α, called Effective Cluster Interactions (ECI), converge to zero as the size and/or distance between points of the cluster increase, and thus Equation 2.6 can be truncated. The ECI implicitly account both for the intra- and inter- sublattice interactions, as well as the effect of atomic relaxations.

The values of the ECI in Equation 2.6 can be obtained from the total energies of a series of structures with various configurations of ions calculated with accurate first-principles methods. This study fit the ECI to the calculated energies by using a linear programming method, both optimizing the least squares differences and maintaining the calculated ground states [43]. For more details on cluster expansions and their applications to metals, oxides, and semiconductors, the reader is referred to the references [34, 37, 39, 44, 45].

2.4 Monte Carlo Statistical Methods

The cluster expansion allows rapid calculation of the energy of any arbitrary ionic arrangement within the host lattice. This feature makes it convenient for use in Monte Carlo simulations to determine finite temperature thermodynamic properties. Within a Monte Carlo simulation, ionic arrangements are sampled in such a way as to obtain a weighted probability distribution expected from statistical mechanics. The output of the Monte Carlo simulations are thermodynamic averages, such as average concentration as a function of chemical potential. Free energy curves can be obtained by numerically integrating the chemical potential using Equation 2.5, with one of the end members as the reference concentration ($x_o = 1$ or 0).

Chapter 3

Phase Separation Tendencies of Aluminum-Doped Transition-Metal Oxides

3.1   Introduction

There has recently been considerable interest in Al-doping of lithium intercalation oxides, (LiMO$_2$, where M is a transition metal). Al substitution of the transition-metal cation has been shown theoretically and experimentally to increase the cell voltage [9]. In addition, Chiang *et al.* [10] have demonstrated the positive effect of Al on the cycle-life and high-temperature stability of Mn-based insertion oxides. Ohzuku *et al.* [11] showed these same effects for Al-doping in layered LiNiO$_2$. Some other advantages of Al are that it is light, non-toxic, and inexpensive.

Because of the interest in Al-doping of lithium insertion electrodes, we have investigated the miscibility of Al in a number of first row transition-metal oxides (Ti, V, Cr, Mn, Fe, Co, Ni, and Cu). Although our results for most systems are based on only a few calculations, we find large positive enthalpies of mixing between LiAlO$_2$ and half of the lithium transition-metal oxides studied (Ti, V, Mn, and Fe), indicating that Al miscibility may be limited in these systems at low processing temperatures. For Li(Al,Co)O$_2$ and Li(Al,Cr)O$_2$, in which mixing enthalpies are small, we calculated the full temperature-composition phase diagrams. For the Al-doped Co system, full miscibility in the range from -173°C to 600°C is predicted. In both systems, Li(Al,Co)O$_2$ and Li(Al,Cr)O$_2$, the formation of γ-LiAlO$_2$ limits Al solubility at temperatures above 600°C.

3.2 Miscibility in Al-Doped Layered Oxides

3.2.1 Formation Energies

The tendency for two compounds to mix can be estimated from their enthalpy of mixing, *i.e.* the enthalpy difference between the mixture and the pure compounds. The enthalpy of mixing for $LiAlO_2$ with another $LiMO_2$ compound is:

$$\Delta H_{mix}(LiAl_{1-y}M_yO_2) = H_{LiAl_{1-y}M_yO_2} - y \cdot H_{LiM_yO_2} - (1-y) \cdot H_{LiAl_{1-y}O_2} \qquad 3.1$$

Positive enthalpies of mixing represent a tendency for phase separation. Negative values indicate the formation of ordered compounds. Only positive values of the mixing enthalpy were obtained for all eight transition-metal oxides studied. However, even when a system has a positive enthalpy of mixing it may still form a solid solution if the temperature is high enough for the entropy contribution to the free energy to compensate for the positive enthalpy $(G \equiv H - T \cdot S)$. In practice, the enthalpy of mixing (ΔH) can be replaced by the internal energy (ΔU) of mixing since the $p\Delta V$ term is usually very small for solid-state reactions $(H = U + P \cdot V)$. Note that mixing is considered for an overall stoichiometry of $LiAl_{1-y}M_yO_2$. The conditions of oxygen partial pressure needed to achieve this average oxidation states for the cations is not computed. When the oxygen partial pressure does not lead to an average valence of 3+ for the cations, other compounds with different valence may form and prohibit mixing. This effect is not investigated here.

We compute the formation energies for a series of compounds with different choices of M, but all with the same layered trigonal α-$NaFeO_2$ structure (space group R$\bar{3}$m). Eight metal oxides were studied (Ti, V, Cr, Mn, Co, Fe, Ni, Cu). For half of the metals examined, including $LiCoO_2$, a well studied and commercially used cathode compound [46, 47], this is the equilibrium structure. All the compounds in Equation 3.1, both the pure end-members and doped materials, were assumed to be in this same structure, even when it is not the experimentally observed crystal structure, in order to isolate the chemical effects from structural factors. Note that whenever $LiMO_2$ does not crystallize the layered α-$NaFeO_2$ structure, our calculated enthalpies of mixing relative to the true experimental structure will

be underpredicted (*i.e.* too small). This is because the experimentally observed structure would then have a lower (more negative) enthalpy than what we calculate for layered $LiMO_2$. Hence from Equation 3.1, the enthalpy of mixing would be higher. While our results only apply directly to mixtures in the layered state, they may also give an indication of the sign of the enthalpy of mixing in other host structures.

Hewston and Chamberland [48] extensively reviewed the crystal structures of the first row of transition-metal $LiMO_2$ compounds. Four (V, Cr, Co, and Ni) of the eight transition-metal oxides studied here and $LiAlO_2$, are stable at room temperature in the α-$NaFeO_2$ crystal structure. $LiNiO_2$ is stable in a Jahn-Teller distorted variant of this structure, having some site disorder between the Li and Ni sites [49]. The other four metal oxides, M = Ti, Mn, Fe, and Cu, have different experimentally observed crystal structures. See the reference [48] for more details.

	Ti	V	Cr	Mn	Fe	Co	Ni	Cu
y=0.3333	337	249	1	148	94	13	25	18
y=0.5000	299	228	14	131	70	28	3	47
y=0.6666	253	229	7	111	44	9	11	17

Table 3.1:   Computed formation energies, in meV/unit cell, for $LiAl_{1-y}M_yO_2$ in the α-$NaFeO_2$ ($R\overline{3}m$) crystal structure.

Total energies for a series of $LiAl_{1-y}M_yO_2$ compounds were calculated with first-principles methods (see Chapter 2). The results of the formation energy calculations are shown in Table 3.1. Pure $LiCoO_2$ can be calculated using a unit cell of four atoms. In order to calculate mixed compounds, larger superstructures must be used. The structures chosen to evaluate the enthalpy of mixing had the smallest unit cells possible for the studied composition (8 or 12 atoms). In addition, these structures had the lowest energy of those calculated for the Li(Al,Co)O_2 system where a more extensive set of structures was investigated (see Section 4.3). All of the formation energies are positive, indicating that thermodynamically, $LiAl_{1-y}M_yO_2$ favors phase separation into $LiAlO_2$ and $LiMO_2$ at low temperature. It is possible, although unlikely, that ordered compounds with larger unit cells

have negative formation energies. Several additional structures were investigated in the Li(Al,Co)O$_2$ system, and all had positive formation energies as well. This implies that these materials will form low temperature miscibility gaps, each separating into the two end-member compounds. At higher temperatures, entropy effects will dominate and the material is expected to transform into a solid-solution state.

3.2.2 Transition Temperatures

The temperatures at which a complete Al-M solid solution can be achieved depend on the mixing enthalpies and may be above the decomposition temperature of the oxide for large positive enthalpies. We can approximately predict the transition temperatures from the calculated formation energies. de Fontaine [39] outlined a variety of free energy calculation methods, comparing their accuracy using the predicted transition temperatures from each method. The transition temperature can be found from the nearest neighbor pair interaction:

$$T_c = \frac{\tau \cdot z^{(1)} \cdot \left|V_1\right|}{k_B} \qquad\qquad 3.2$$

where T_c is the transition temperature, τ is a transition parameter, $z^{(1)}$ is the coordination number, V_1 is the nearest-neighbor pair interaction, and k_B is Boltzmann's constant. For these six-fold two dimensional lattices where $z^{(1)} = 6$, the best-known fit gives a transition parameter of $\tau = 0.0602$.

To obtain the nearest-neighbor pair interactions, V_1, a cluster expansion with a single nearest-neighbor ECI was fit to the enthalpies of mixing for each of the eight transition metals. These ECI are shown in Table 3.2. Once the nearest-neighbor ECI have been obtained, the transition temperature can be approximated using Equation 3.2. The eight predicted transition temperatures are shown in Figure 3.1.

	Ti	V	Cr	Mn	Fe	Co	Ni	Cu
V_1: First nn ECI	-75	-59	-1.2	-33	-17	-2.8	-4.7	-6.9

Table 3.2:   Nearest-neighbor ECI in meV for layered LiMO$_2$, fit with five structures.

We can relate the transition temperature directly to the enthalpy of mixing at $y_{Al} = 0.5$ by a constant C_1:

$$C_1 = \frac{k_B \cdot T_c}{\Delta H} = \frac{0.6062 \cdot 6 \cdot |V_1|}{\Delta H} \qquad\qquad 3.3$$

The values obtained for the constant for each dopant are shown in Table 3.3. From this data we can extrapolate a rule of thumb showing that full miscibility occurs above temperatures T:

$$k_B T > 0.9 \cdot \Delta H \qquad (\text{at } y_{Al} = 0.5) \qquad\qquad 3.4$$

This approximation is quite close for Ti, V, Mn, and Fe, the four metals with fairly high transition temperatures. For the four metals with much lower transition temperatures, the approximation does not hold as well. Small variations in the energy calculations will translate to a large difference in this factor for systems with small formation energies. Therefore this rule of thumb seems to work only for systems with large formation energies.

	Ti	V	Cr	Mn	Fe	Co	Ni	Cu
C_1	0.86	0.90	0.30	0.87	0.85	0.34	4.75	0.50

Table 3.3:   Parameter relating ΔH at y=0.5 to $k_B T_c$.

For the $Li(Al,M)O_2$ compounds for which $LiMO_2$ is not layered (Ti, Mn, Fe, and Cu), the estimate will go up if the true equilibrium structure of $LiMO_2$ were accounted for. The rough prediction of T_c for $Li(Al,Co)O_2$ from Equation 3.2 agrees well with the more exact result from the calculated phase diagram described in more detail in Section 3.3.3 — they differ by roughly 15%. This confirmation suggests that our approach provides a reasonable estimate of the temperature at which complete solid solution can be reached.

The size difference between the metal ion and dopant Al ion will effect the miscibility of Al. The larger the metal ion, the greater the size difference between it and the Al ion. A large size difference with the substituting ion would create more lattice strain and therefore a greater tendency for phase separation. Figure 3.1 show these ionic sizes for each transition
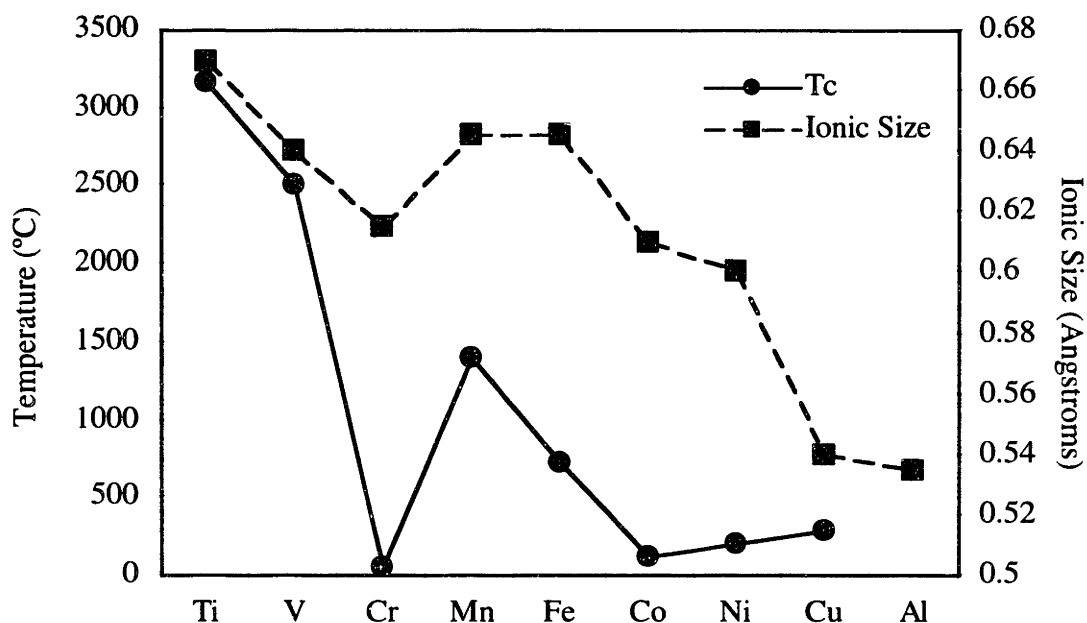
Figure 3.1: Estimated temperature above which complete solid solution can be reached in layered $Li(Al,M)O_2$ plotted next to ionic size of the M^{3+} ions. Ionic radii are from Shannon [50].

metal (The ions are in the 3^+ valance state with octahedral coordination, from Shannon [50]). As can be seen from the plot, a definite correlation exists between the transition temperature and ionic size — the four largest ions, Ti, V, Mn, and Fe, have the highest transition temperatures. Chemical effects such as electronic bonding and magnetic effects will alter the interactions as well so that T_c is not exactly determined by the physical size of the ions. For example, Cu^{3+} is much smaller than Cr^{3+}, Co^{3+}, or Ni^{3+}, and yet $Li(Al,Cu)O_2$ has the greatest T_c of the four. Mn^{3+} and Fe^{3+} are the same size but they differ in transition temperature. However, an overall trend clearly exists between ionic size and transition temperatures.

3.3 Li(Al,Co)O₂ Detailed Analysis

While zero temperature energy calculations can give indications of (im)miscibility, a complete temperature-composition calculation of the free energy is required to predict the temperature dependence of solubility limits. For one system, $LiAl_{1-y}Co_yO_2$, we have

performed a complete phase diagram calculation.

Experimentally, α-LiAlO$_2$ is observed to crystallize in the α-NaFeO$_2$ structure below 600°C [51, 52]. Above this temperature, γ-LiAlO$_2$ is stable in the tetragonal crystal structure (space group P4$_1$2$_1$2). The major difference between the two structures is that the Al ions are tetrahedrally coordinated in the tetragonal structure, while they are octahedrally coordinated in the layered structure. LiCoO$_2$ forms in the layered α-NaFeO$_2$ crystal structure for all temperatures.

When α-LiAlO$_2$ and LiCoO$_2$ mix below 600°C it is reasonable to assume that the α-NaFeO$_2$ crystal structure is maintained so that Al and Co ions mix only on the (111) planes of the rocksalt structure, while the Li plane remains perfect in composition. An extensive study on the Li(Al,Ni)O$_2$ system by Ohzuku et $al.$ confirms this separation of ions into separate planes [53]. No disorder between the Li plane and the (Al,Co) plane was allowed. The disorder of Al and Co was restricted to a two-dimensional triangular lattice of sites. Adding inter-plane interactions in the cluster expansion did not significantly change the results, hence these were neglected. More details on cluster expansions can be found in Chapter 2.

Total energies for 9 different compositions of LiAl$_{1-x}$Co$_x$O$_2$ in the α-NaFeO$_2$ structure were calculated using first-principles methods. The corresponding formation energies, found using:

$$\Delta E_{mix}(LiAl_{1-x}Co_xO_2) = E_{LiAl_{1-x}Co_xO_2} - x \cdot E_{LiCo_xO_2} - (1-x) \cdot E_{LiAl_{1-x}O_2} \qquad 3.5$$

are plotted in Figure 3.2. The formation energies for this system are positive, but quite small. From the formation energies, a 2-D cluster expansion was calculated with three nearest-neighbor pairs and two triplets. The resulting ECI from the cluster expansion are shown in Figure 3.3. The total least squares error of the fit was 0.75 meV. Figure 3.2 also shows the predicted energies from the cluster expansion along with the original calculated values.
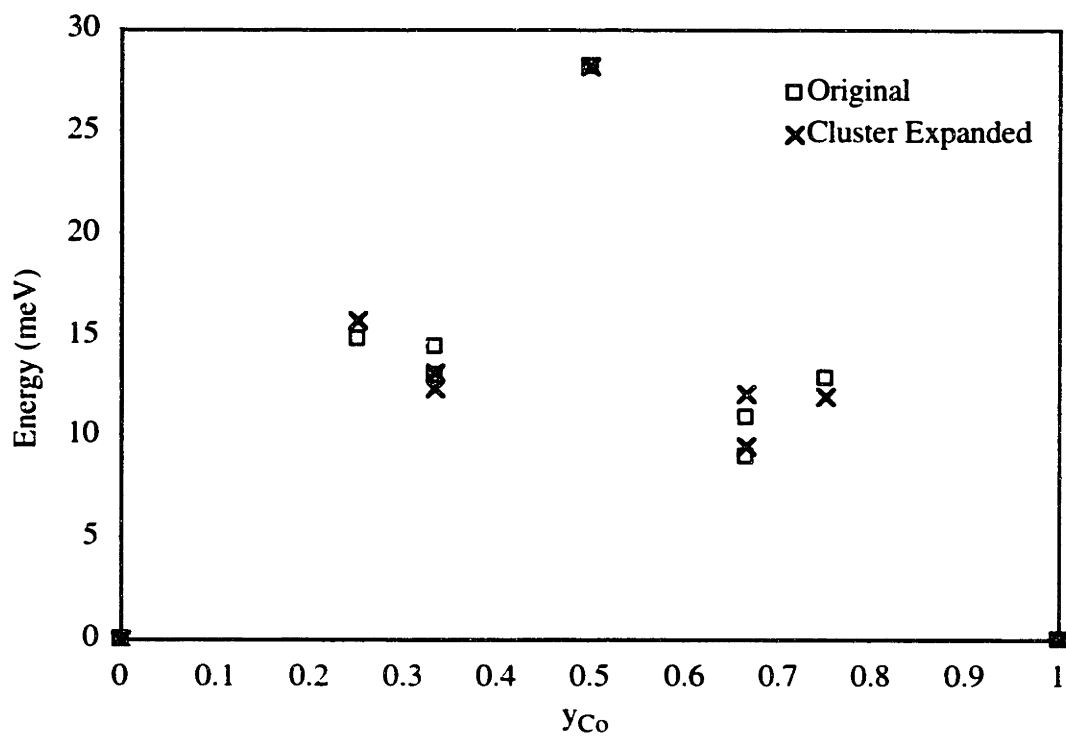
Figure 3.2:   Computed formation energies and energies predicted from the cluster expansion, in meV, for $LiAl_{1-y}Co_yO_2$ in the α-$NaFeO_2$ ($R\overline{3}m$) crystal structure.
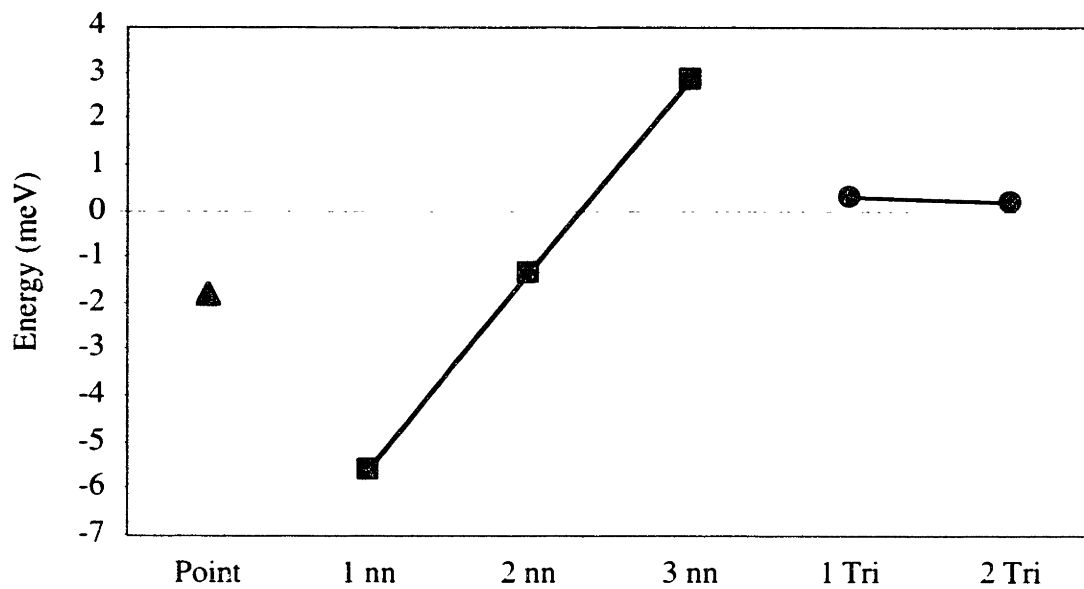

Figure 3.3:   ECI for $Li(Al,Co)O_2$ 2-D cluster expansion.

3.3.1 Miscibility Gap

The low temperature miscibility gap was calculated by running a 2-D Monte Carlo analysis with the ECI from the cluster expansion. A set of chemical potentials with corresponding composition at different temperatures was obtained from the Monte Carlo simulation. A lattice size of 36 by 36 atoms in the Al-Co plane and 4,000 Monte Carlo passes were performed after 1,000 equilibration passes.

The free energy of the layered structure as a function of composition was calculated through numerical integration. Two sets of Monte Carlo runs were done at each temperature, one starting at each end composition, y=0 (LiAlO$_2$) and y=1 (LiCoO$_2$). These these two sets of chemical potentials, $\mu(\sigma)$, for each temperature were integrated to determine the free energy g(σ) at each composition σ ($\sigma = 2y - 1$):

$$g_{left} = \int_{-1}^{\sigma} \mu(\sigma) \cdot d\sigma$$

$$g_{right} = \int_{\sigma}^{1} \mu(\sigma) \cdot d\sigma$$

3.6

From the free energies and the chemical potentials, the grand canonical potentials, w(σ), were calculated for each point:

$$w(\sigma) = g(\sigma) - \mu(\sigma) \cdot \sigma$$

3.7

Comparing the grand canonical potentials, we were then able to find the common tangent for the free energy curves, and the edges of the miscibility gap are then σ_{left} and σ_{right}. The calculated miscibility gap is shown in Figure 3.4.

3.3.2 Two-Phase Region above 600°C.

Free energies for all compositions in the layered phase were determined by Monte Carlo simulations using the grand canonical ensemble on a system of 576 (8 x 8 x 7) Co-Al sites. At each temperature and chemical potential, 1000 equilibration passes per lattice site were

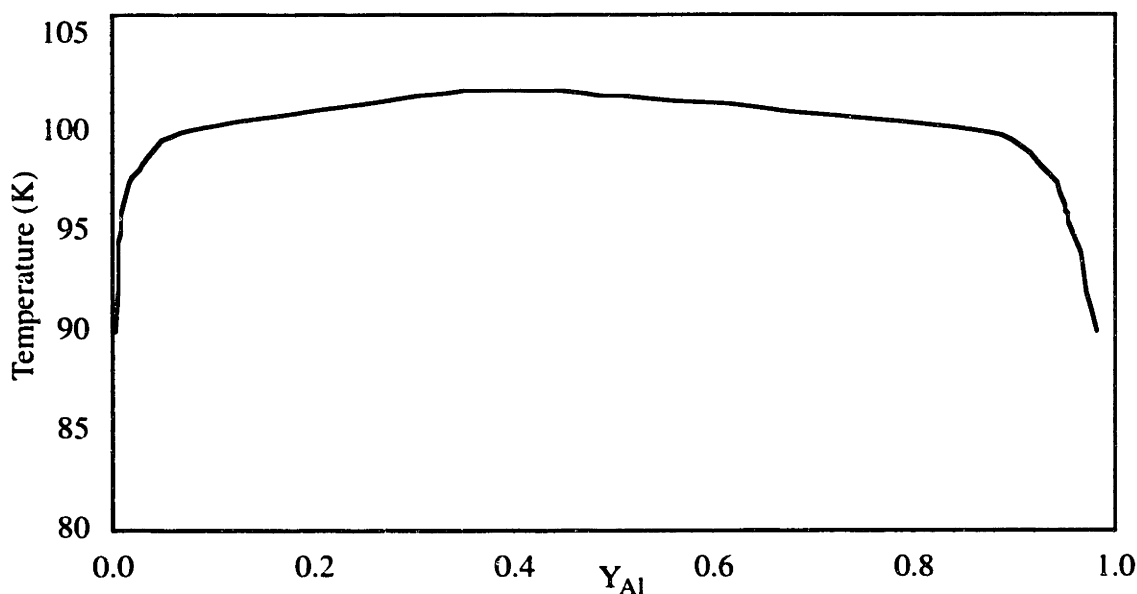Figure 3.4:   Calculated miscibility gap for $LiAl_yCo_{1-y}O_2$.

performed after which sampling occurred over an additional 4000 Monte Carlo passes as in the previous section. Free energies were found by performing thermodynamic integration of the chemical potential as a function of composition.

γ-LiAlO₂ as a line compound

In principle, a separate cluster expansion is required for the tetragonal parent lattice of γ-$LiAlO_2$. However, we calculated the energy for substituting Co in the tetragonal structure and found the energies for these compounds to increase very rapidly with y_{Co}. The formation energies for mixed tetragonal $Li(Al,Co)O_2$ ranged from 300 to 800 meV per unit cell and the total energies for tetragonal structures were greater by 850 to 1500 meV per unit cell than the total energies of the layered structures at the same composition, as shown in Table 3.4 and Table 3.5. We therefore concluded that Co is not miscible in the tetragonal phase and that γ-$LiAlO_2$ can be treated as a stoichiometric line compound.

To obtain the *free* energy of γ-$LiAlO_2$ relative to α-$LiAlO_2$, the total energies at zero K were compared — the calculated difference is 165 meV. We can assume that this difference is the enthalpy difference as well, as all the calculations are done at 0 K and the $p\Delta V$ term is

	LiAlO$_2$	25% Co	50% Co	75% Co	LiCoO$_2$
Total Energy Tetragonal (eV)	-28.95	-27.96	-27.03	-26.97	-26.74
Total Energy Layered (eV)	-29.12	-28.81	-28.52	-28.25	-27.97

Table 3.4: Comparison of total energies per unit cell for tetragonal versus layered structures at 0 K.

	LiAlO$_2$	25% Co	50% Co	75% Co	LiCoO$_2$
Formation Energy Tetragonal (meV)	0	440	818	319	0
Formation Energy Layered (meV)	0	15	28	13	0

Table 3.5: Comparison of formation energies per unit cell for tetragonal versus layered structures at 0 K.

usually very small for solid-state reactions $(H = U + P \cdot V)$. Because the two phases are in equilibrium, the free energies at the transition temperature, $T_c = 600°C$, must be equal:

$$G_\gamma(T_c) = G_\alpha(T_c) \qquad \qquad 3.8$$

Also, we assume that the heat capacities of α-LiAlO$_2$ and γ-LiAlO$_2$ are the same and thus the difference between the two structures' entropies is constant and equal to the value at the transition temperature:

$$S_\gamma - S_\alpha = \frac{H_\gamma - H_\alpha}{T_c} \qquad \qquad 3.9$$

Then by subtracting the free energy relations from $G = H - TS$ for each structure we obtain:

$$G_\gamma - G_\alpha = H_\gamma - H_\alpha - T(S_\gamma - S_\alpha) \qquad \qquad 3.10$$

Finally, we find the free energy of γ-LiAlO$_2$ relative to α-LiAlO$_2$:

$$G_{\gamma-\text{LiAlO}_2} = 165\text{meV} \cdot \left(1 - \frac{T}{873 \text{ K}}\right) \qquad 3.11$$

Thus we have the free energy for the tetragonal phase, modeled by a simple relation between temperature and the energy difference between the two phases.

Determining the edge of the two-phase region

The location of the common tangent between the free energies of the two phases, γ-LiAlO$_2$ and solid-solution layered Li(Al,Co)O$_2$, defines the edge of the two-phase region. The left side, pure γ-LiAlO$_2$, is simply a line compound and so the left edge of the two-phase region is at $y_{Co} = 0$ or $\sigma = -1$. ($\sigma = 2y - 1$) The right edge of the region is the composition where the tangent line between the free energy curve of the layered structure and the energy of the line compound cross the layered curve. The slope of the free energy curve, $g(\sigma)$, is the chemical potential, $\mu(\sigma)$. Numerically solving Equation 3.12 for σ gives the right edge of the miscibility gap for each temperature. The edge of the two-phase region can be seen in the full phase diagram, Figure 3.5.

$$
\begin{aligned}
g(\sigma) &= \mu(\sigma) \cdot \sigma + \text{intercept}(\sigma = 0) \\
\text{intercept}(\sigma = -1) &= \text{intercept}(\sigma = 0) + \mu(\sigma) \cdot (-1) \\
\text{intercept}(\sigma = -1) &= g(\sigma) - \mu(\sigma) \cdot \sigma + \mu(\sigma) \cdot (-1) \\
\text{intercept}(\sigma = -1) &= g(\sigma) - \mu(\sigma) \cdot \sigma - \mu(\sigma) \\
\text{intercept}(\sigma = -1) &= g(\sigma) - \mu(\sigma) \cdot (\sigma + 1) \\
F_{\gamma-\text{LiAlO}_2} &= g(\sigma) - \mu(\sigma) \cdot (\sigma + 1)
\end{aligned}
\qquad 3.12
$$

3.3.3 Phase Diagram

The phase diagram obtained by combining the miscibility gap results in Figure 3.4 and the results for the two phase region is given in Figure 3.5. Within the Li(Al,Co)O$_2$ phase diagram, the lower temperature miscibility gap is symmetric and peaks at about -173°C. Owing to the low temperature of this miscibility gap there is no experimental data with which to compare this part of the result. At 600°C the transformation of layered α-LiAlO$_2$ to the tetragonal

phase, in which no Co dissolves, creates a new two phase region on the Al rich side. Above 600°C the solubility of Al into layered $LiCoO_2$ actually decreases with temperature due to the increasing stability of γ-$LiAlO_2$. Such a case of retrograde solubility, while unexpected, is not all that uncommon.

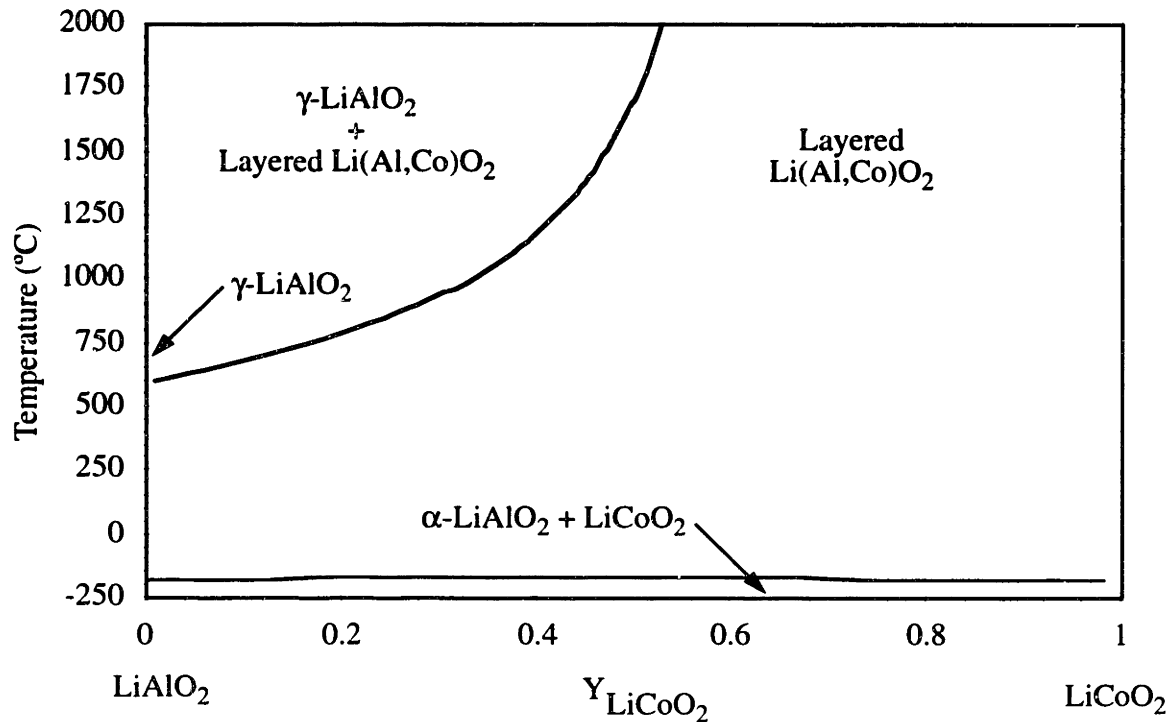Figure 3.5:   Calculated phase diagram for $LiAl_{1-y}Co_yO_2$.

Comparison to Experiments

Initial experiments on the $Li(Al,Co)O_2$ system done by Nazri et al. [54] found the solubility limit for the formation of solid solutions of Al in $LiCoO_2$ to be around 25% when processed at 750°C. However, γ-$LiAlO_2$ was one of the starting materials, and so it is difficult to assess if a true solubility limit was reached or whether the material had not been treated long enough to reach equilibrium. A second study, by Alcántara et al. [55], agrees with our results; they found no traces of γ-$LiAlO_2$ at 700°C with composition up to 70% Al. Recent experiments by Jang et al. [56] at 800°C have confirmed the existence of a two-phase region at $LiAl_{0.75}Co_{0.25}O_2$, and a solid solution at $LiAl_{0.25}Co_{0.75}O_2$. However, they also find traces of

the tetragonal phase at 50% Co, where the results of this study show that the two-phase region ends at about 30% Co at this temperature. Because the results of the experimental studies disagree with each other and with our calculated results, it is difficult to decide whether these differences are due to our calculations or experimental discrepancies, such as incomplete equilibrium. Further experimental investigation of the phase diagram in this region is therefore warranted.

It is interesting to note that this two-phase region occurs in other Al-doped layered oxides as well. Chiang *et al.* find that in $Li(Al,Mn)O_2$ [10, 57], small amounts of Al can be incorporated into the layered structure, but at greater Al concentrations γ-$LiAlO_2$ forms. Their results indicate a solid solubility of Al in the layered phase of about 5-7% at 950-1000°C. This very small solubility can be explained by considering the miscibility results from Section 3.2. These results indicate that below about 1130°C, $Li(Al,Mn)O_2$ would phase separate. In this case, the material would phase separate into $LiMnO_2$ and γ-$LiAlO_2$, since the processing temperatures are above the α- to γ- transition temperature of 600°C. An Al solid-solubility limit between 20% and 30% was found for $Li(Al,Ni)O_2$ [58] at 700°C again much smaller than for $Li(Al,Co)O_2$.

Tetrahedral Sites

Alcántara *et al.* [55] have speculated that at low Al concentration, tetrahedral occupation by Al in $LiAl_{1-y}Co_yO_2$ may limit the material's reversibility. They have found through powder X-ray diffraction and verified using NMR that at 20% Al content, one third of the Al ions (6.1% of all metal ions) sit in tetrahedrally-coordinated positions in the Li plane. Although Al is known to exhibit tetrahedral coordination with oxygen in other compounds, in the fully lithiated layered structure, the Al ions would sit very near to the Li ions, which are in the octahedral positions, as shown in Figure 3.6. With smaller lithium concentrations, the octahedral sites immediately next to the tetrahedral Al ions could be vacant, leaving enough rooms for Al ions without being so close to another ion. Fully relaxed calculations of the energy of those candidate structures reveal that the results for $Li_{0.25}Al_{0.25}Co_{0.75}O_2$ with the Al ions in tetrahedral locations are in fact quite close to the energy of the structure with Al
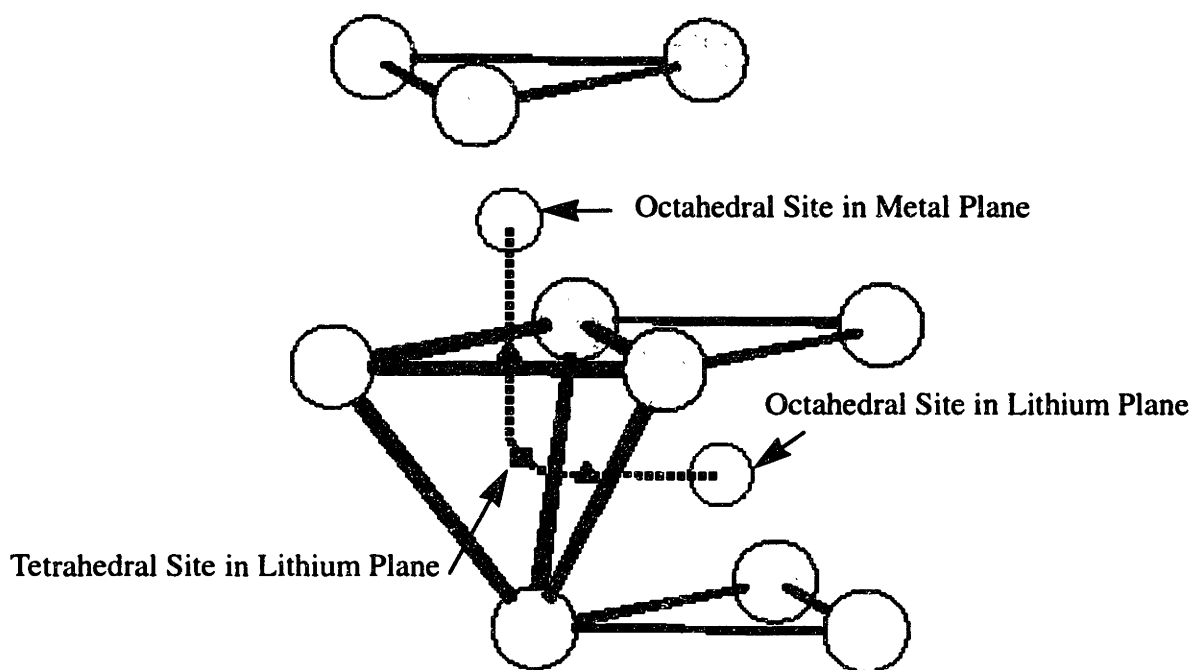
34

Figure 3.6:   Tetrahedrally coordinated and octahedrally coordinated positions in the
               α-NaFeO$_2$ layered structure.

octahedrally coordinated in the metal plane, as shown in Table 3.6. With such a small energy difference, interactions more complicated than nearest neighbors could play a role, and thus more complicated defect structures could form. In addition, significant occupation of the tetrahedral site by Al ions could occur due to entropy effects. For simplicity, in the fully lithiated structure with Al tetrahedral we only allowed the volume of the cell to relax. The resulting energies are much higher than the corresponding layered structure with only octahedral Al. Though we have not been able to confirm the experimental results at 100% Li concentrations using first-principles methods, Al migrating to tetrahedral positions would result in a decrease in lithium ion diffusivity and, consequently, the observed poor reversibility found when Li(Al,Co)O$_2$ is used as a cathode material.

Oxygen Defects

Another possible source for the discrepancy between theoretical and experimental results could be due to oxygen defects. More details on this analysis are included in Chapter 5.

	Al in Tetrahedral position	Al in Octahedral Position
25% Li	-23.783	-23.886
	-23.864	
100%Li	-26.606[a]	-28.815

Table 3.6:   Formation energies, in meV per unit cell, for Al in tetrahedral positions in the composition $Li_yAl_{0.25}Co_{0.75}O_2$. [a]Only volume is relaxed.

3.4   Li(Al,Cr)O$_2$ Phase Diagram

Aluminum solubilities similar to our results for Li(Al,Co)O$_2$ have been found for Al doped LiCrO$_2$. In Li(Al,Cr)O$_2$, experimental studies have shown that 60% Al substitution was reached for processing temperatures up 920°C [58]. Above this temperature, γ-LiAlO$_2$ forms.
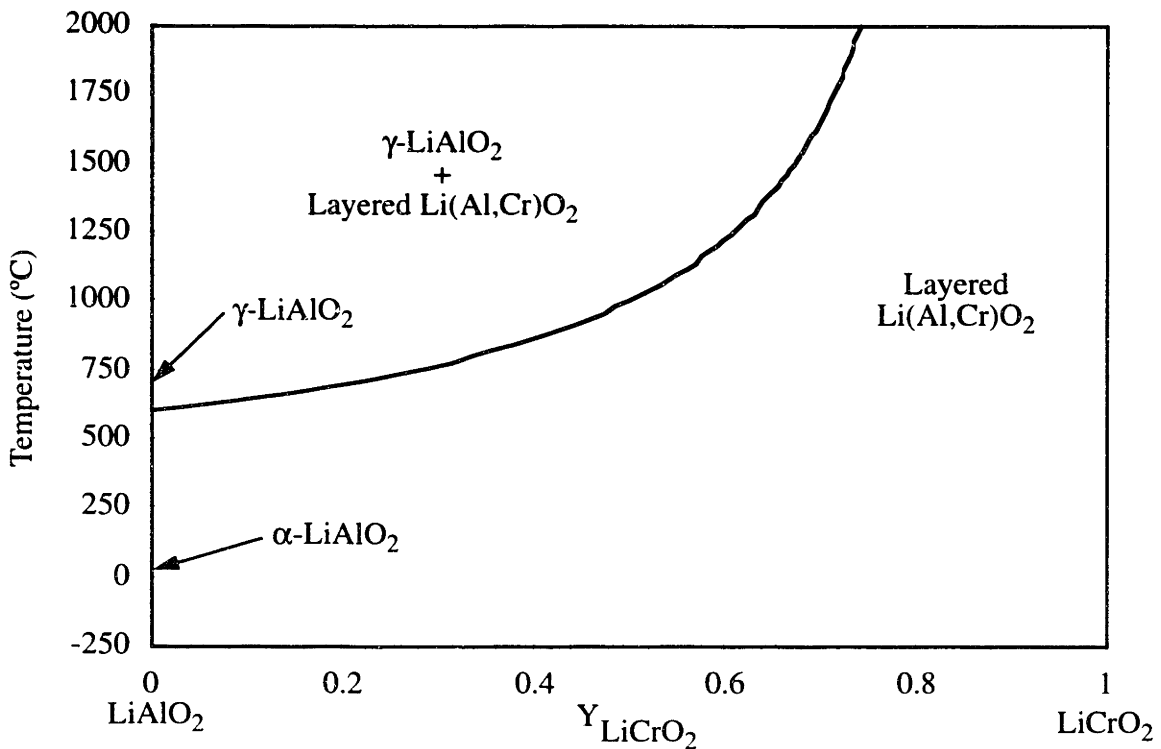

Figure 3.7:   Calculated phase diagram for $LiAl_{1-y}Cr_yO_2$.

For Li(Al,Cr)O$_2$ a phase diagram can be easily calculated. Since the mixing enthalpies in the layered structure (Table 3.1) are particularly small in this system, the free energy of the layered phase may be approximated with an ideal solution model without any significant loss in accuracy. Combining these energies with Equation 3.11 for the free energy of γ-LiAlO$_2$ results in the phase diagram of Figure 3.7. As in Li(Al,Co)O$_2$ the solubility at high temperature is limited by the stability of γ-LiAlO$_2$. This agrees very well with experiment. Our results find an edge to the two-phase region at Al-doping levels of 55%. Poeppelmeier *et al.* [58] find at 60% Al content, the material remains a layered solution below 920°C, while above this temperature, it decomposes to γ-LiAlO$_2$ and the layered solid solution Li(Al,Cr)O$_2$.

3.5 Conclusions

The energy calculations described in this chapter show that layered transition-metal oxides can be doped with Al to possibly improve cathode battery performance, but the amount of Al that can be stably accommodated depends on the material and processing temperatures. In Li(Al,M)O$_2$, three of the eight transition metals studied (M = Ti, V, Mn) phase separate at temperatures below 1000°C. For one transition-metal oxide, Li(Al,Fe)O$_2$, the miscibility gap peaks within normal processing temperatures, at about 450°C. The other four oxides (M = Cr, Co, Ni, Cu) have low temperature miscibility gaps, but form solid solutions at room temperature. Therefore five of the eight first row transition metals studied, (Cr, Co, Ni, Cu, and Fe) can be doped with Al at typical processing temperatures.

A full temperature-composition phase diagram was calculated for LiAl$_{1-y}$Co$_y$O$_2$ and complete Al-Co miscibility is found between -173°C and 600°C. Above 600°C, Al-doping in LiCoO$_2$ is limited by the formation of γ-LiAlO$_2$. A temperature-composition phase diagram was also calculated for LiAl$_{1-y}$Cr$_y$O$_2$. Complete miscibility is found below 600°C, and again above 600°C, Al-doping is limited by the formation of γ-LiAlO$_2$. For all oxides which have substantial solubility with LiAlO$_2$ in the layered phase, reduced solubility should be expected above 600°C due to the formation of γ-LiAlO$_2$. The possibility of Al ions sitting in tetrahedral positions was investigated, but could not be confirmed with first-principles energy calculations.

Interestingly, our calculation for $Li(Al,Co)O_2$ shows complete solubility at intermediate to low temperatures. This realization may pave the way for $LiAl_{1-y}Co_yO_2$ mixtures with a high degree of Al substitution. Al doping will reduce the total theoretical capacity by moving some of the voltage to a very high potential [9], but currently commercial batteries based on the $LiCoO_2$ system use only about half of the theoretical capacity. Substitution of the non-oxidized fraction of Co ions by Al should result in significant cost and weight savings.

Chapter 4

Voltages in Mixed Oxides for Lithium Batteries

4.1   Introduction

Lithium-metal oxides with a mixture of cations on the metal site, $Li(M,M')O_2$ are currently of much interest for rechargeable battery cathodes as they may offer the possibility of improved electronic and physical properties over those of single-metal oxides such as $LiCoO_2$, $LiNiO_2$ and $LiMn_2O_4$. For example, initial studies have shown that doping Co in $LiMn_2O_4$ results in an increase in both voltage and cycling performance over pure $LiMn_2O_4$ [60]. Co doping in $Li(Ni,Co)O_2$ has been shown to stabilize the layered structure and allow for longer cycle life before breakdown [61].

The principles that determine the change in electrochemical properties when two metals are mixed on the transition metal site are currently poorly understood. For example, whereas one might expect the Li intercalation potential of a mixed-metal system to lie between that of the two pure metal oxides, results for $Li(Ni,Co)O_2$ indicate that this simple prediction is incorrect [61]. For most compositions in the $Li(Ni,Co)O_2$ system, the Li intercalation potential lies below the composition-averaged value for $LiCoO_2$ and $LiNiO_2$. Understanding the "mixing rules" for electrochemical properties and structural stability is therefore crucial for the intelligent design of optimized intercalation oxides.

We first investigated doping in Mn-based spinels ($LiM_yMn_{2-y}O_4$) with five transition metals (M = Cr, Fe, Co, Ni and Cu). While the calculated average voltages were less than the experimental results for all dopants except Cu, both results followed similar trends with increasing atomic number. An in-depth analysis was performed on the mixed layered structure

Li(Al,Co)O$_2$. The energetics of different lithium sites were investigated and Li sites with one or two Al nearest neighbors were found to be less stable than those surrounded entirely by Co. This unexpected stability leads to an initial decrease in the Li intercalation voltage, though the average voltage over the entire Li range is raised by Al substitution. We also studied the effect of short-range cation ordering on the intercalation curve for Li(Al,Co)O$_2$. One of the advantages of a computational modeling study is that the level of Al-Co homogeneity can be fully controlled. With the cations in fully homogenous solid solutions, the voltage curve was linear. A step in the voltage curve appeared when small, nanosized clusters were introduced.

4.2 Doped Manganese Spinels

Lithium manganese oxide spinels, LiMn$_2$O$_4$, have been extensively investigated as cathodes for rechargeable lithium batteries. Compared with LiCoO$_2$, LiMn$_2$O$_4$ is a low cost and less toxic alternative. However, the battery capacity of LiMn$_2$O$_4$ fades out during charge cycling around 4V. Several transition-metal substituted spinels, LiM$_y$Mn$_{2-y}$O$_4$ (M = Co, Cr, Ni, Mg, and Ga) have shown better cycling performance around the 4 V plateau compared with the pure LiMn$_2$O$_4$. Recent studies by Kawai et al. [60, 62, 63] have shown that some doped spinels have part of their voltage curve above 5 V. New electrolytes have allowed the operation of these materials at such high voltages.

4.2.1 Review of experimental results

Manganese spinels, both doped and pure, show plateaus in the intercalation curve. Upon charging, pure LiMn$_2$O$_4$ exhibits a plateau at ca. 4.1 V [6]. Doping these materials has been shown experimentally to affect both the voltage and extent of these plateaus. An extensive study by Kawai et al. [64] in the Li(Co,Mn)$_2$O$_4$ system has shown that as the amount of Co doping increases, the extent of the original plateau decreases and a new, much higher plateau appears ca. 5.1 V increasing smoothly with Co content. At 25% Co doping, Li$_2$CoMn$_3$O$_8$, the voltage curve remains at the lower plateau for half of the Li extraction and steps up to the

5.1 V plateau for the remainder (see Figure 4.1 from [65]). Upon reaching a 50% Co dopant level, LiCoMnO$_4$, the 4.1 V plateau is almost negligible, and the entire intercalation curve is essentially along the upper plateau.
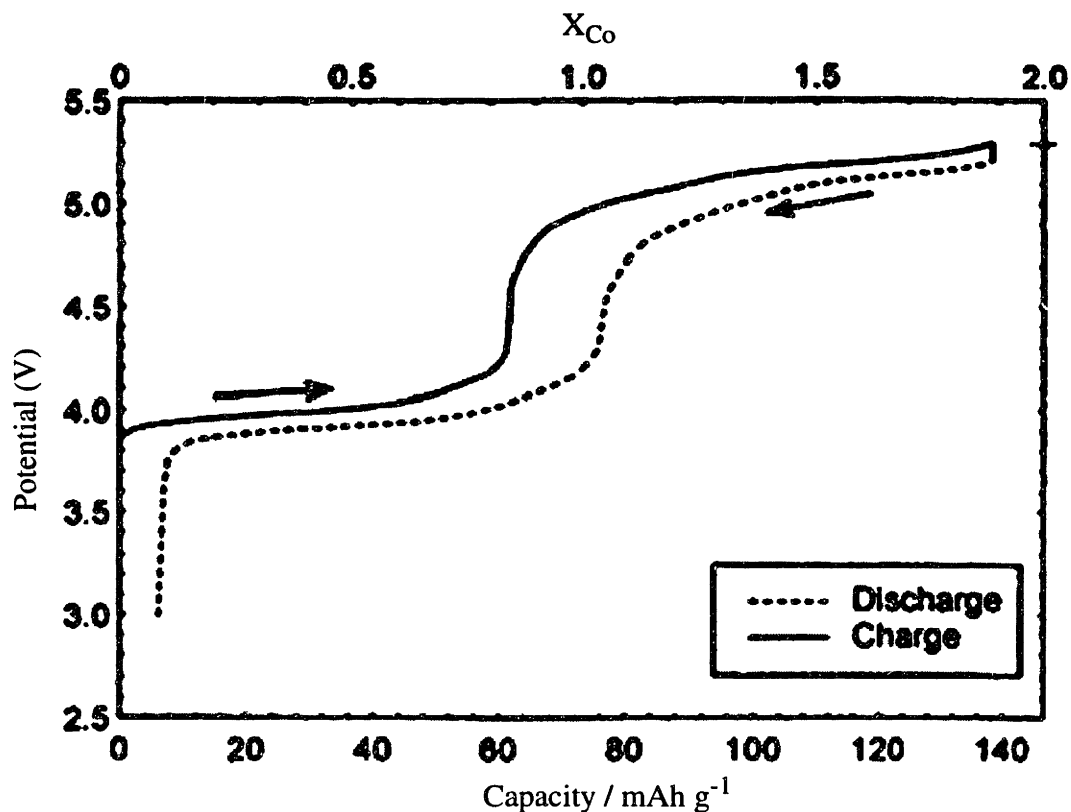
Figure 4.1:   Experimental potential profile during the first cycle for Li$_{2-x}$CoMn$_3$O$_8$ by Kawai *et al.* [65].

Similar results have been reported for doping Mn with Fe [63], Cu [66, 67], Ni [7], and Cr [8, 68]. For all of these transition metals, a new plateau appears at higher voltages. A summary of these results is shown in Table 4.1. Reports of aluminum-doped manganese by Song *et al.* [69] show the decrease in the capacity at the original plateau, but these studies do not investigate the effects above 4.5 V and so show no experimental results on the possible 5 V regions of Al doping.

41

	Cr	Fe	Co	Ni	Cu
Upper Plateau (eV)	4.8 V	4.9 V	5.0 V	4.7 V	4.9 V

Table 4.1: Experimental voltage plateaus for doped Mn spinels (from references [8, 63, 60, 7, 66] respectively)

4.2.2 Voltages

In order to computationally determine both the high and low plateaus found experimentally we calculated the average voltages of both the doped Mn spinels. Using first-principles methods based on LDA, the total energies were calculated for five different dopants with three Li compositions, all at the composition $Li_xMMn_3O_8$, with $x_{Li} = 0$, 1, and 2. All the calculations were spin-polarized and the unit cells were based on eight oxygen and four metal ions. The number of Li ions used varied with Li concentration. For more details on the first-principles methods used, see Chapter 2. To determine the average voltage over a Li compositions range, we took the difference between the energy values at the ends of the range and subtracted the energy of a Li ion in solid Li. However, this gives us only the *average* voltage over the composition range — it tells us nothing about how the voltage behaves therein.

	Cr	Fe	Co	Ni	Cu	Mn
Voltage from $X_{Li} = 0$ to 1	4.36 V	4.55 V	4.85 V	4.56 V	4.98 V	4.29 V
Voltage from $X_{Li} = 1$ to 2	3.84 V	4.00 V	3.77 V	3.94 V	4.14 V	3.59 V

Table 4.2: Calculated average voltages for each side of the $X_{Li} = 1.0$ step in doped and pure manganese spinels, $Li_xMMn_3O_8$, M = Cr, Fe, Co, Ni, Cu.

The average voltages are shown in Table 4.2. They are also shown graphically alongside the experimental results in Figure 4.2. As can be seen from Figure 4.2, the calculated results tend to be lower than experiments for both the upper and lower plateaus, as reported previously in [22]. However, the trend moving along the first row in the periodic table is

consistent between the experimental and calculated results for the higher portion of the voltage curve. The voltages increase from Cr to Co, drop for Ni, and then rise again for Fe. While our data follows experiment along the periodic table, the order of the voltages is not consistent with experimental results. Ni is the lowest in the doped spinels for experimental results, while it is the same as Fe and higher than Cr in our calculations. The results for the
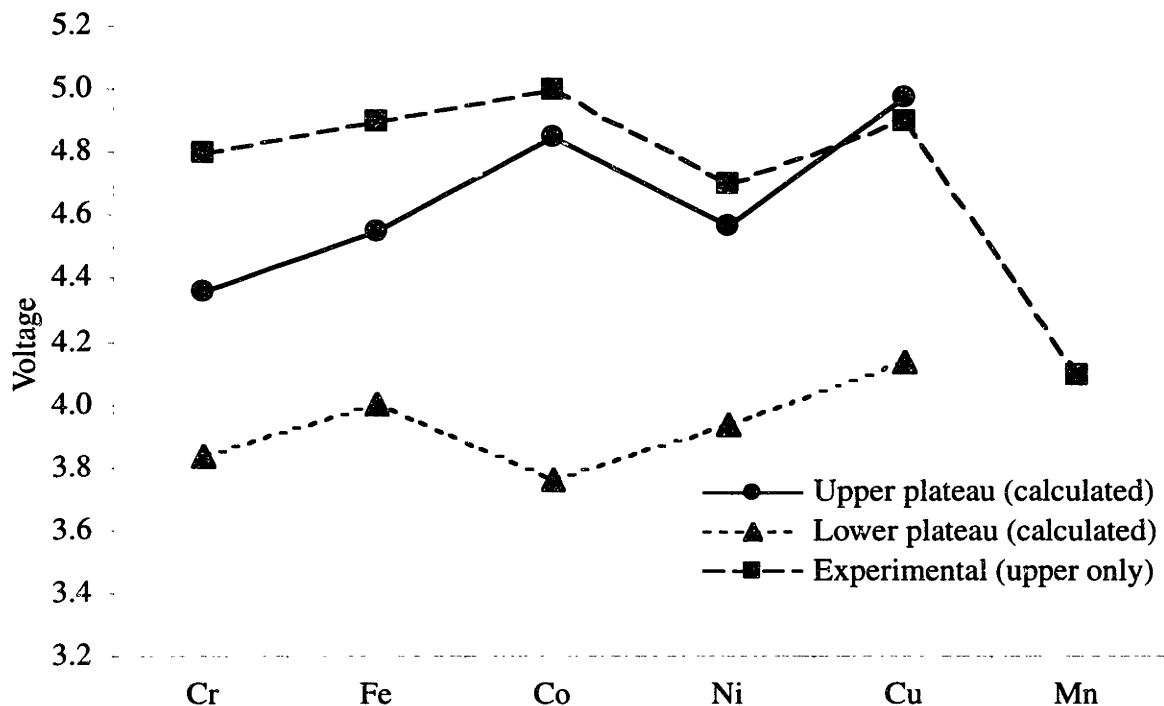
Figure 4.2: Average voltages for doped manganese spinels $Li_xMMn_3O_8$. The upper plateau ranges from $x_{Li} = 0$ to 1 while the lower plateau spans $x_{Li} = 1$ to 2.

	Cr	Fe	Co	Ni	Cu	Mn
Voltage from $X_{Li} = 0$ to 1	4.27 V	4.31 V	4.90 V	4.16 V	5.02 V	4.29 V
Voltage from $X_{Li} = 1$ to 2	3.99 V	2.85 V	4.54 V	3.86 V	4.78 V	3.59 V

Table 4.3: Calculated average voltages in pure spinels ($Li_xM_4O_8$).

	Cr	Fe	Co	Ni	Cu
Calculated Average Voltage	4.10 V	4.28 V	4.31 V	4.25 V	4.56 V
Predicted Average Voltage	4.04 V	3.76 V	4.33 V	3.98 V	4.42 V

Table 4.4: Calculated and predicted average voltages for the mixed spinels $X_{Li} = 0$ to 2 ($Li_xMMn_3O_8$). The predicted values are found by averaging the values for the voltages over the entire Li composition range in the two constituent pure spinels.

Cu doped spinel are inconsistent as well. Cu has the highest calculated plateau, but is lower than Co experimentally.

One possible source of discrepancy between the calculated and experimental results is that the experiments were performed by a variety of groups. Differences in preparation and testing of the samples may very well produce slightly different results. Because we are comparing potentials that vary by only 0.1 or 0.2 volts, differences in processing may explain some of the inconsistencies.

The average voltages over the same Li composition ranges were also calculated for each of the pure spinels, $Li_xM_4O_8$, M= Cr, Fe, Co, Ni, Cu, and Mn, as shown in Table 4.3. By averaging the two average voltage over the entire Li concentration range studied, we can predict the average voltage in the mixed structures, as shown in Table 4.4. In comparing the calculated average voltages to the predicted values, we can see that the predicted voltages are lower than the calculated ones in four out of the five dopants. For the the Co doped spinel, the predicted voltage is 0.02 V above the calculated value. Thus, in general, mixing tends to increase voltage more than simply averaging the constituents would predict.

4.2.3 Ordering

In transition-metal doped spinels, the octahedral metal sites are occupied by more than one type of cation. Though the distribution of cations is random at high temperatures, they are often observed to be ordered at low temperatures. Many doped spinels with composition $Li_2MM'_3O_8$ exhibit 1:3 cation ordering on the octahedral 16d sites [65]. However, initial investigations by Kawai et al. [60, 63] do not show definitive evidence for ordering in Fe-

doped or Co-doped Mn spinels. This may be because Co, Fe, and Mn have very similar atomic scattering factors. In these materials with similar scattering factors, ordering is difficult to characterize with structure refinement in powder XRD patterns.

To investigate the possibility of ordering in Mn-based spinel structures, we calculated the formation energies for 5 different transition-metal doped Mn spinels. All five doped materials, $Li_2MMn_3O_8$, (M = Cr, Fe, Co, Ni, Cu), have positive formation energies as shown in Table 4.5. Positive formation energies indicate a tendency for phase separation. These results imply that doped Mn spinel structures would not form 1:3 cation ordering. However, the mixing enthalpies are quite small for Cr and Co. Other magnetic and electronic effects may come into play and affect the interaction of the different ions. Experimental research is continuing in this area to determine the extent of ordering in different doped systems.

Fitting a nearest neighbor interaction and combining it with the Bragg-Williams model:

$$T_c = \frac{6|V_1|}{k_B}$$

4.1

where T_c is the transition temperature, V_1 is the nearest neighbor interaction, and k_B is Boltzmann's constant, we can roughly predict the transition temperature for mixing in these doped spinels. The formation energies for Ni and Fe doped Mn oxides are approximately the same, near 100 meV. These energies would correspond to a miscibility gap of about 900°C at 50% doping level. However, at the 25% doping level, experiments on these systems do not report any appearance of phase separation during XRD examination for processing temperatures of 650°C to 800°C [7, 63]. For the Co and Cr doped spinels, the predicted transition temperatures for phase separation would be 350°C and -40°C respectively. These are below normal processing temperatures and so the phase separation tendencies would not effect the making of these materials. For $Li_2CuMn_3O_8$ the formation energy is quite high. Using the simple pair interaction model, we would predict that below 2750°C the Cu doped material would phase separate. Experimental studies do not discover phase separation at processing temperatures well below the predicted transition temperatures for Cu doped Mn spinels either [66, 67]. Clearly this model for predicting transition temperatures needs to

examined. The Bragg-Williams approximation could be incorrect for this system or our formation energies could be inaccurate.

	Cr	**Fe**	**Co**	**Ni**	**Cu**
Formation Energy (meV)	20	101	53	100	261

Table 4.5: Formation energies in meV per metal atom for spinel $Li_2MMn_3O_8$ structures, M = Cr, Fe, Co, Ni, and Cu.

4.3   Voltages in Layered Li(Al,Co)O$_2$

The Li(Al,Co)O$_2$ system was chosen for several reasons. Initial results show that the LiCoO$_2$ intercalation curve is raised by aluminum substitution [56]. The similarity of Al and Co ions in these lithium metal oxides also makes Al an attractive choice for doping: the end members, α-LiAlO$_2$ and LiCoO$_2$, have the same crystal structure, layered α-NaFeO$_2$ (though for α-LiAlO$_2$ this is true only below 600°C - see Section 3.3 for more details), and the metal ions are close in size. These similarities remove the complications of phase transitions and lattice strain when varying doping content.

The layered α-NaFeO$_2$ structure (space group R$\bar{3}$m), is shown in Figure 4.3. The structure consists of alternating hexagonal lithium and metal planes, separated by planes of oxygen. Each lithium site is surrounded by six oxygen anions and six metal cations, three above and three below.

Methodology

The lithium potential in the intercalation oxide is directly proportional to its chemical potential:

$$V(x) = -\frac{\mu_{Li}^{cathode}(x) - \mu_{Li}^{anode}}{zF} \qquad 4.2$$

where z is the number of electrons transferred and F is the Faraday constant. In this work, μ_{Li} on the anode side is assumed to be constant and equal to the energy of Li metal. Though Li
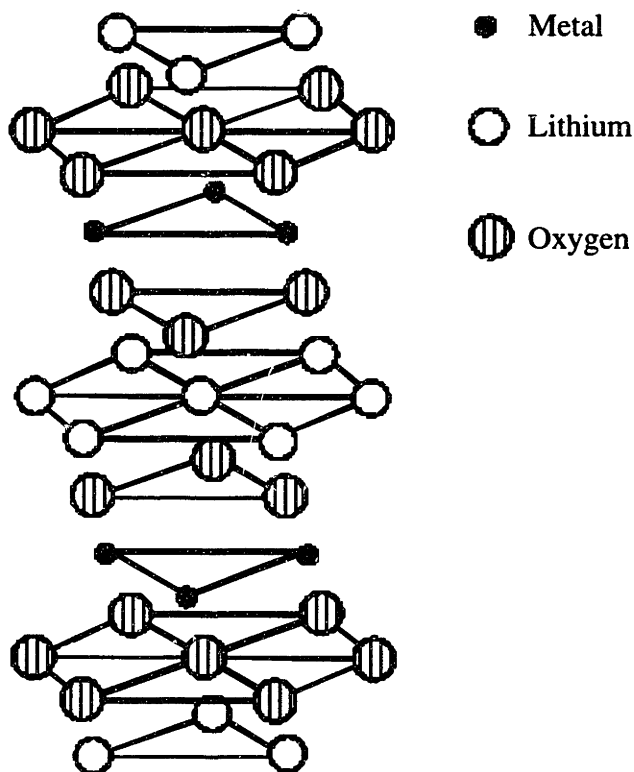
Figure 4.3:   The layered α-NaFeO$_2$ crystal structure (space group R$\bar{3}$m)

metal is not used as the anode in practical secondary batteries, it is a useful reference state and is therefore used in our calculations as well as in experimental test cells. To calculate $\mu_{Li}(x)$ in the cathode, a model for the free energy as a function of Li concentration is needed.

First-principles energy methods were used to calculate the energies of 64 different structures in the Li$_x$Al$_y$Co$_{1-y}$O$_2$ system ranging in composition from $x_{Li} = 0$ to $x_{Li} = 1$ and $y_{Al} = 0$ to $y_{Al} = 1$. From these total energies, the formation energies for each "binary" system were calculated. (See Equation 3.5) The binary systems consisted of maintaining a constant x or y, set to 0 or 1, while allowing the other variable to change. The four systems are LiAl$_y$Co$_{1-y}$O$_2$, Al$_y$Co$_{1-y}$O$_2$, Li$_x$AlO$_2$, and Li$_x$CoO$_2$. The formation energy results for these systems are shown in Figures 4.4 to 4.7. Note that the formation energies for LiAl$_y$Co$_{1-y}$O$_2$, shown in Figure 4.6, are all positive. This implies that there is a tendency for phase separation since the mixed structures have a higher formation energy than the end-members and are therefore unstable. (See Section 3.3.1 for more details.) We also calculated energies of

structures in the middle of these four edges, structures with both x_{Li} and y_{Al} between 0 and 1. These "inner points" are not shown.

For this study a coupled-cluster expansion was used, varying both the Li and the Al-Co composition. The coupled cluster expansion is an extension of the binary cluster expansion described in Chapter 2. Here, there are two occupation variables, one for the Li-vacancy sublattice, σ_i, and one for the Al-Co sublattice, δ_i. The dependence of the structure's energy on the configuration of both Al-Co and Li-vacancy can then be expanded in terms of polynomials of these discrete occupation variables similar the simpler Equation 2.6.

$$E = V_0 + V_{Li-pair} \cdot \sigma_i \cdot \sigma_j + V_{Metal-pair} \cdot \delta_k \cdot \delta_l + V_{Coupling-pair} \cdot \sigma_i \cdot \delta_k + ... \qquad 4.3$$

The products in Equation 4.3 of the occupation variables correspond to Li-vacancy interactions, Al-Co interactions, and interactions between Li and the metal sublattice. Though there are four components in this system (Li, vacancy, Al, Co) the separation of these elements into two distinct sublattices allows the system to be sectioned and treated as a binary cluster expansion. The two different sets of components do not intermix and cross-over to the other sublattice — they remain solely in sites in their own lattice. Therefore we can treat the system with only the two independent sets of occupation variables. For more information on coupled-cluster expansions, see [70].

This cluster expansion contained 26 ECI based on the calculated energies of the 64 different structures. These ECI represent nearest-neighbor pairs and triplets within each sublattice, as well as pairs, triplets, and quadruplet terms coupling the Li and metal sublattices. The results of the cluster expansion are shown by the ECI in Figure 4.8. It is evident that the energy of a specific configuration depends strongly on the coupling terms - the location of the Li ions relative to the number of Co and Al nearest neighbors.

The results of the cluster expansion itself are also shown by the energies that the ECI predict for different structures. The cluster expanded energies of the structures calculated from first principles are shown in Figures 4.4 to 4.7, alongside the calculated energies. For some compositions the fit is quite good. For example, in Li_xCoO_2, many structures were calculated and the least-squares error between the predicted energies and the calculated energies is

0   0.2   0.4 X_{Li} 0.6   0.8   1

0

-50

Energy (meV)

-100

-150

-200

-250

□ Original
✗ Cluster expanded

Figure 4.4:   Formation energies and cluster expanded energies for Li_xCoO_2.

50

40

30

20

Energy (meV)

10

0

0   0.2   0.4 X_{Li} 0.6   0.8   1
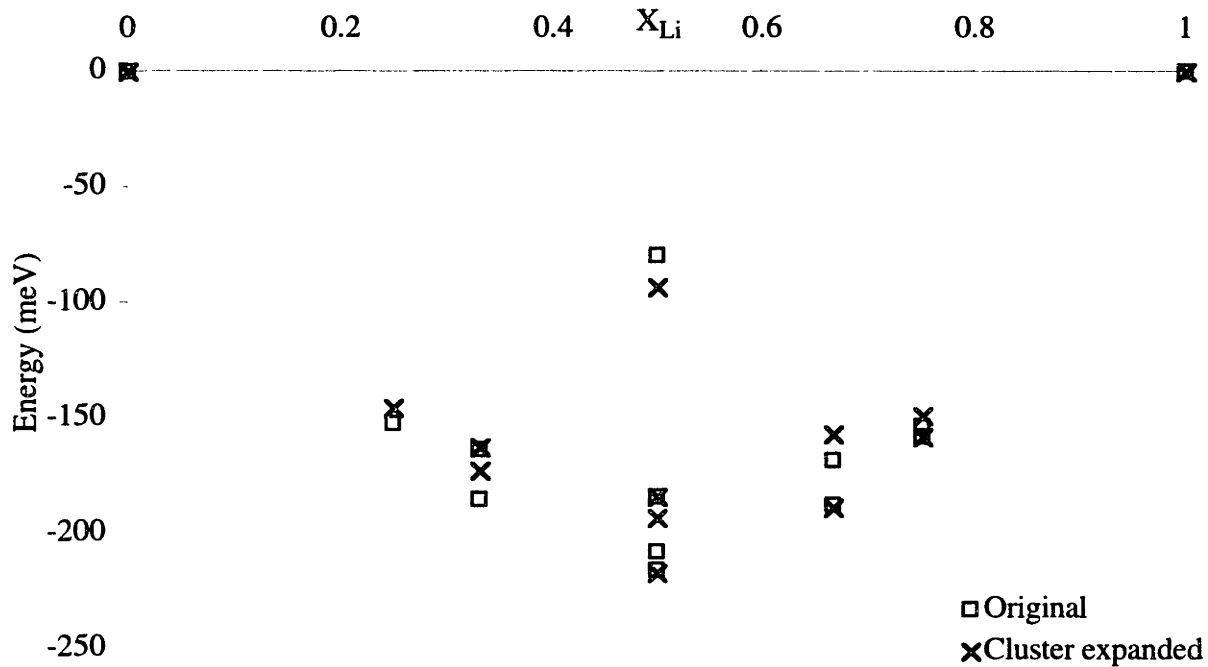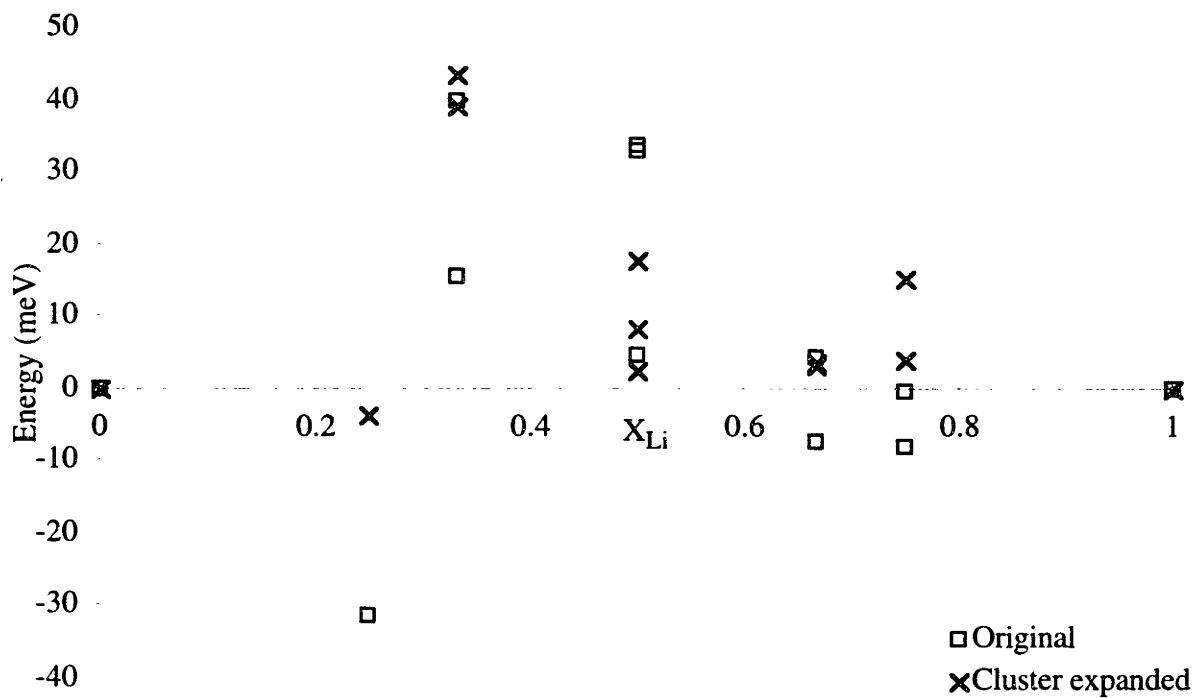
-10

-20

-30

-40

□ Original
✗ Cluster expanded

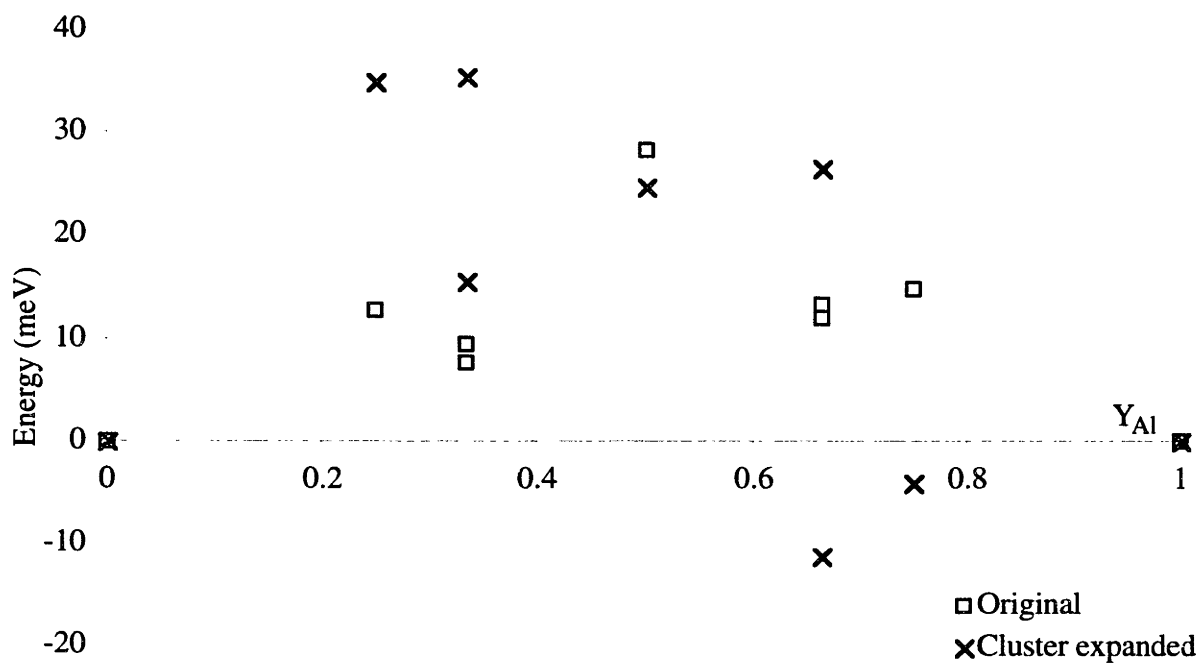Figure 4.5:   Formation energies and cluster expanded energies for Li_xAlO_2.

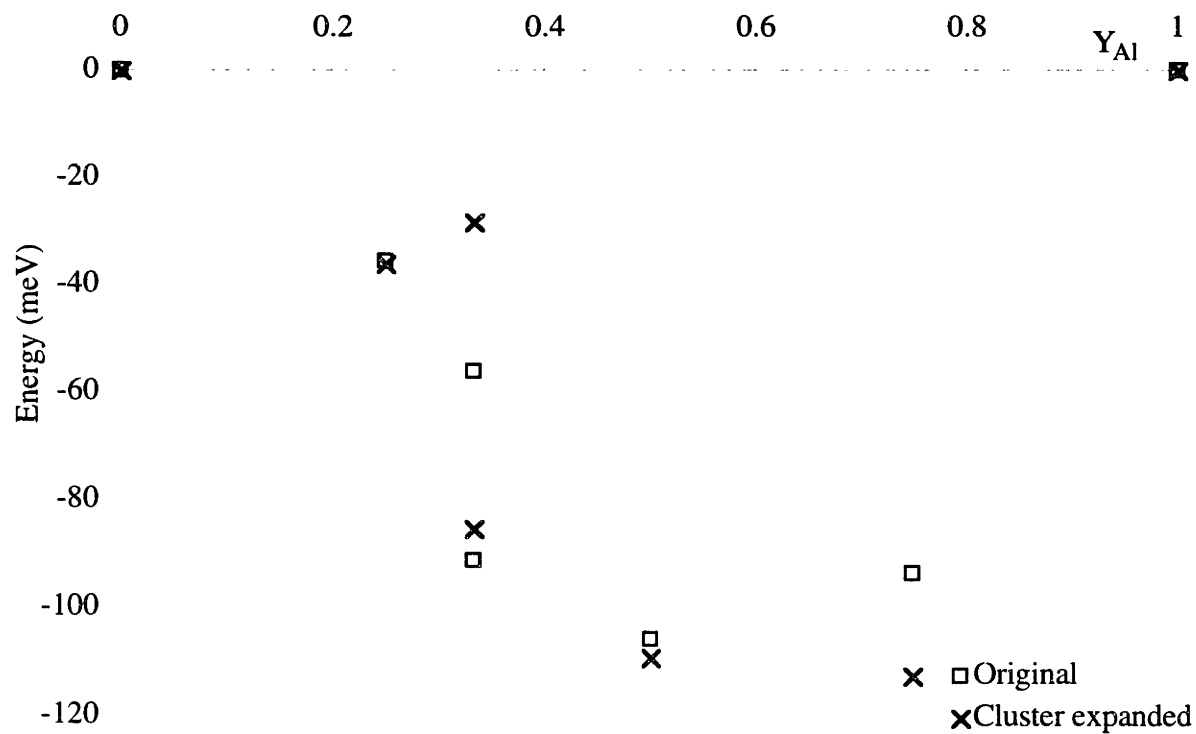Figure 4.6:   Formation energies and cluster expanded energies for $LiAl_yCo_{1-y}O_2$.

Figure 4.7:   Formation energies and cluster expanded energies for $Al_yCo_{1-y}O_2$.
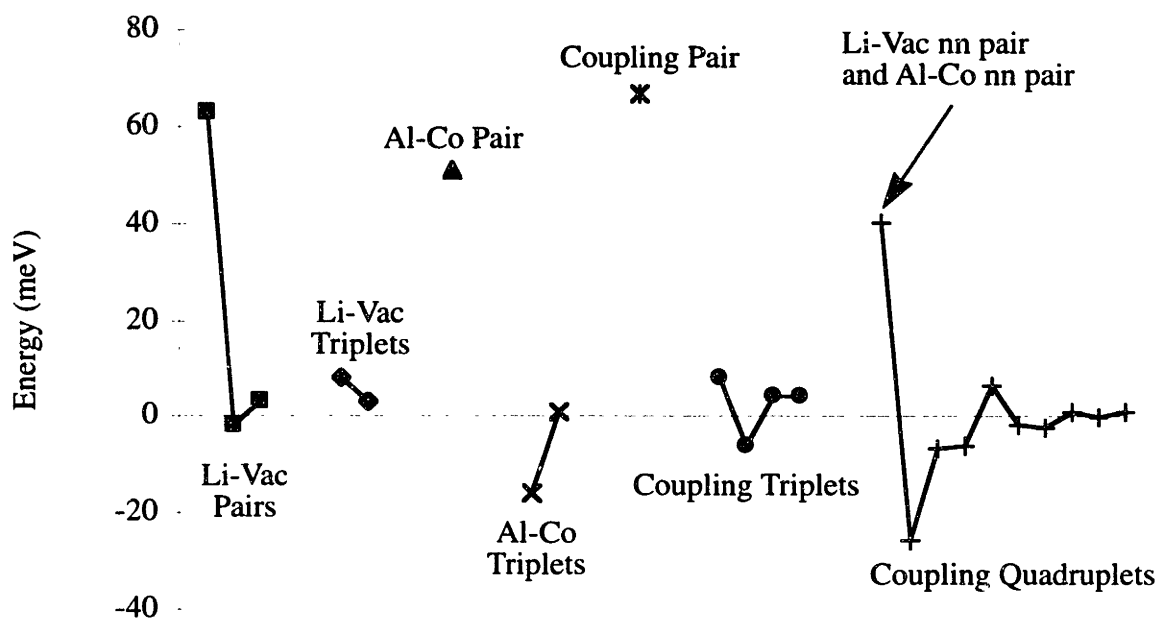
Figure 4.8: ECI from the coupled cluster expansion for $Li_xAl_yCo_{1-y}O_2$.

7.7 meV. A similar least-squares error is obtained for the structures not included in the fit. However, for the delithiated material, $Al_yCo_{1-y}O_2$, getting the cluster expansion to simply converge was very difficult. One calculated energy had to be removed from the fit entirely and even then the cluster expansion had a least-squares error of 13 meV for the included structures. For the four binary systems along the edges (x = 0, x = 1, y = 0, or y = 1), the overall least-squares error was 14 meV. The ground-state line was maintained for three of the four systems, Li_xAlO_2, Li_xCoO_2, and $Al_yCo_{1-y}O_2$. For $LiAl_yCo_{1-y}O_2$, the ground-state line was not maintained. Two structures that had a positive formation energy based on first-principles calculations had a negative stable formation energy using ECI predictions. However, they are stable by only 10 to 20 meV. The energies of the structures with intermediate compositions in both Al-Co and Li were more poorly predicted. The least-squares error of the seven intermediate structures included in the fit was 23 meV (0 < x < 1 and 0 < y < 1). However, the least-squares error of the intermediate structures *not* included in the fit was 220 meV. Including these four structures prevented the cluster expansion from converging at all. The overall error of the included structures was 16 meV, and the error for all

51

64 structures was 60 meV.

By calculating the ECI, we parameterized the energy and thus we can determine the energy at any composition. Monte Carlo simulations use these ECI to find a set of Li chemical potentials and corresponding compositions and temperatures for any configuration of Al and Co on the cation sublattice in the layered α-NaFeO$_2$ structure. Using Equation 4.2 and the chemical potential from the Monte Carlo simulations, the voltage can be determined as a function of x_{Li} at any temperature and Al-Co composition or configuration. The Li$_x$(Al,Co)O$_2$ system has disorder on both the Li and the Co/Al sublattice. While the Li disorder is equilibrated in the simulation, the Al-Co sublattice is frozen into a particular configuration. This is consistent with the expected low mobility of Co and Al at room temperature.

The effect of short range order on the intercalation curve was found by systematically varying the degree of cation clustering from random solid solution to microsegregated Al. In this manner, the intercalation properties of Li$_x$Al$_y$Co$_{1-y}$O$_2$ as a function of Al-Co arrangement were determined. During the Monte Carlo simulation both the occupation of each Li site and each site's relation to the local arrangement of Al and Co ions were recorded. This site data allows the determination of the preferred Li environments as a function of voltage.

4.3.1 Site Preference

To study the site preference of Li ions during intercalation, Monte Carlo simulations were run with varying degrees of Al-Co clustering. Within the layered material, Li ions have six metal nearest-neighbors, three in the metal plane above, and three in the plane below (see Figure 4.9). In the mixed oxide, a single Li site can have from zero to six Al nearest neighbors, with the remaining sites filled by Co ions. In a random solid solution, the number of Li sites in each type of environment is statistically determined.

As the material is charged, the Li ions preferentially leave sites based on the sites' relative energies. During charging, the Li composition decreases and the sites with higher energy (lower potential) empty first, while lower energy sites (higher potential) remain filled.

Figure 4.10 represents the type of occupied Li sites as characterized by the number of Al nearest neighbors. For clarity in the graph, sites with 3 Al nn to 6 Al nn were not included, as
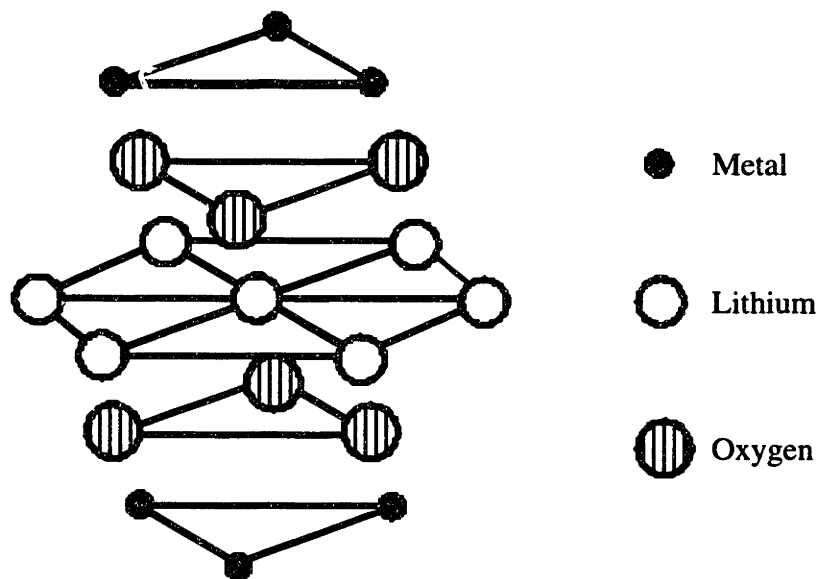
Figure 4.9:   Li site and its Al-Co nearest neighbor environment.

the percentage of these in the random mixture was small and the results did not contribute to the site preference conclusions. These results are based on a simulation with a random solid solution of Al and Co and where the Li configuration is always fully equilibrated. The total number of each type of site is statistically determined based on the composition of the material. Adding all seven types of Li sites (zero to six Al nearest neighbors) totals to 100%. As can be seen in the right side of the diagram, Li ions fill all possible sites at $x_{Li} = 1$, and so all the percentages (including the 3 to 6 Al nn sites not shown) add to 100%.

Interestingly, upon delithiation Li ions first vacate sites with one and two Al nearest neighbors, remaining in the locations completely surrounded by Co ions. The rate of departure of Li ions from a particular site can be seen from the slope. Previous calculations [71] indicate that the theoretical average voltage of pure Li_xAlO_2 is 5.4 V, versus 3.7 V for pure Li_xCoO_2. A higher average potential implies a lower energy — a greater potential is needed to give the Li ions enough energy to leave that environment. From a simplified chemistry standpoint, one might suspect that as the number of Al nearest neighbors increases around a Li ion, the energy of the site would decrease (i.e. Li becomes more difficult to remove). By this reasoning, one would expect that upon delithiation of $Li(Al,Co)O_2$, Li is first removed from sites surrounded by only Co and subsequently from sites surrounded by more Al. As shown in Figure 4.10 this
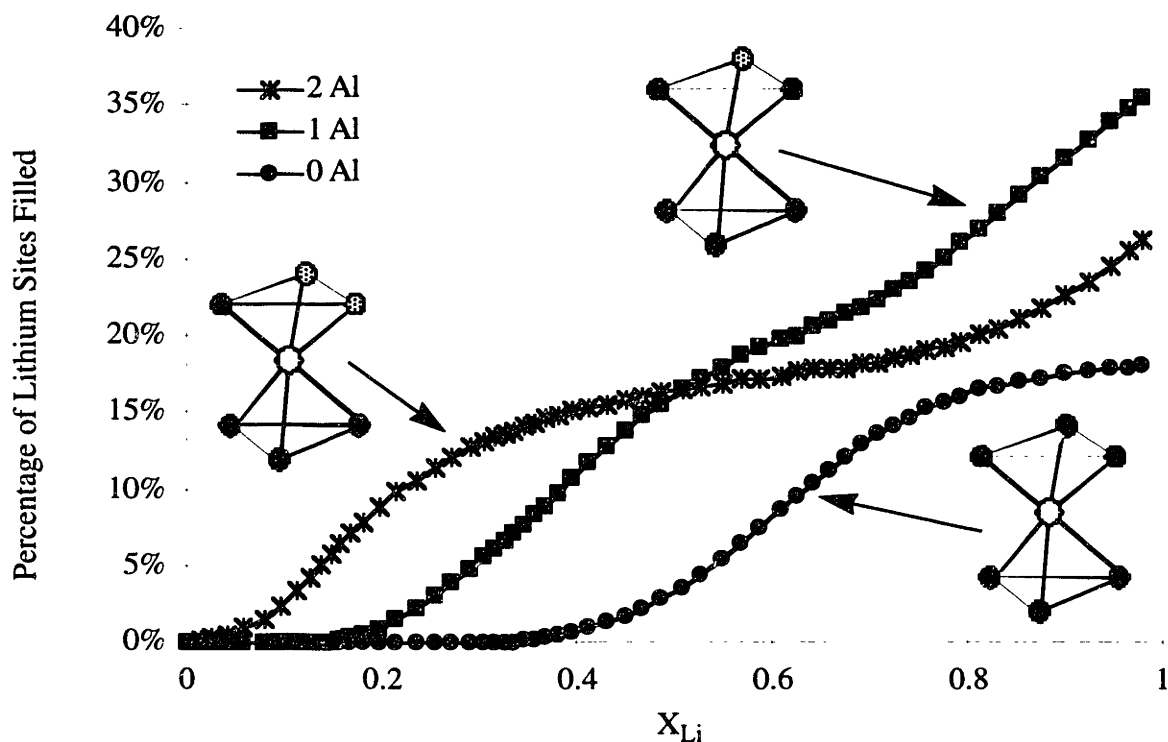
Figure 4.10: $Li_xAl_{0.25}Co_{0.75}O_2$ in random solid solution. Fraction of Li sites broken down by number of Al neighbors. (3-6 Al nn not included)

is not the case. Li actually leaves first from the sites with one and two Al ions before it is removed from the sites surrounded by six Co ions. It is believed that this is due to the difference in relaxation around each site. When a Li site is surrounded by one or two Al ions, the symmetry of the site is broken. Li-Al and Li-Co bonds, while similar in length, are not identical. The calculated bond lengths for Li-Al and Li-Co in $LiAlO_2$ and $LiCoO_2$ are shown in Table 4.6. Their difference is about 1.8%, enough to distort the octahedron surrounding the Li ion. This distortion may actually raise the energy of the site and hence lower the potential at which Li can be removed.

First-principles methods were used to directly calculate the energies of structures with the same Al-Co arrangement but different Li configurations. First, two different structures with a single Li ion removed were examined. The location of the resulting vacancy determined the energy. These two structures were of composition $Li_{.875}Al_{.125}Co_{.875}O_2$. The Li sublattice was composed of seven Li ions and a single vacancy: $Li_7AlCo_8O_{16}$ (31 ions). A third structure was

54

	Bond Length (Å)
Al-Li in LiAlO$_2$	2.82
Co-Li in LiCoO$_2$	2.77

Table 4.6:   Bond length of Al-Li and Co-Li in the fully relaxed LiAlO$_2$ and LiCoO$_2$ structures, respectively.

examined where instead of comparing energies when moving a single vacancy, a single Li ion was moved. This third structure was of composition $Li_{.25}Al_{.25}Co_{.75}O_2$. Here there are 3 vacancies and a single Li ion: $LiAlCo_3O_8$ (13 ions).

The energy results shown in Table 4.7 support the cluster expansion and verify that sites with six Co nearest neighbors have a lower energy for a Li ion, (or a higher energy for a vacancy) than those surrounded by one or two Al ions. Note that the energy difference by moving a single Li ion for all three structures is about 300 to 400 meV. Structures with lower energies represent more stable configurations, therefore as Li is removed from the structure, Li ions remain in the Co surrounded site, leaving a vacancy in the higher energy sites with Al nearest neighbors. When a totally delithiated structure is filled with Li, the Li ions fill the sites completely surrounded by Co before entering some of the sites with one or two Al nearest neighbors. Of course, sites surrounded by all Al ions will fill before any of these, but here we are only examining those sites with few Al neighbors to determine the effect of symmetry breaking on energy.

The difference in energy between the pure Co sites and ones with 1 or 2 Al nearest neighbors is reflected in the intercalation curves for these compounds. Figure 4.11 shows the intercalation curves for two Al/Co solid solutions, one with 5% Al substitution and the other with 25% Al. Though the higher Al substitution increases the average voltage more when measured over the entire Li composition range, at high Li concentrations the voltage curve starts lower for the system with high Al content. The increased Al content creates more one- and two- Al neighbor Li sites and this a higher number of sites with greater energy. The Li sites with a greater energy need a lower voltage to remove the Li. Therefore as the percentage of Al is increased, the starting voltage in fully lithiated material decreases. Unfortunately,

	Types of Sites	6 Co nn site filled by:	Energy
Structure a	5 Co nn & 6 Co nn	Li	-219.742
"	5 Co nn & 6 Co nn	Vacancy	-219.415
Structure b	4 Co nn & 6 Co nn	Li	-220.113
"	4 Co nn & 6 Co nn	Vacancy	-219.817
Structure c	4 Co nn & 6 Co nn	Li	-95.193
"	4 Co nn & 6 Co nn	Vacancy	-94.749

Table 4.7: Calculated energies, in eV, for
a) $Li_{.875}Al_{.125}Co_{.875}O_2$, with 1 vacancy and 7 Li ions (31 ions total);
b) $Li_{.875}Al_{.125}Co_{.875}O_2$, with 1 vacancy and 7 Li ions (31 ions total); and
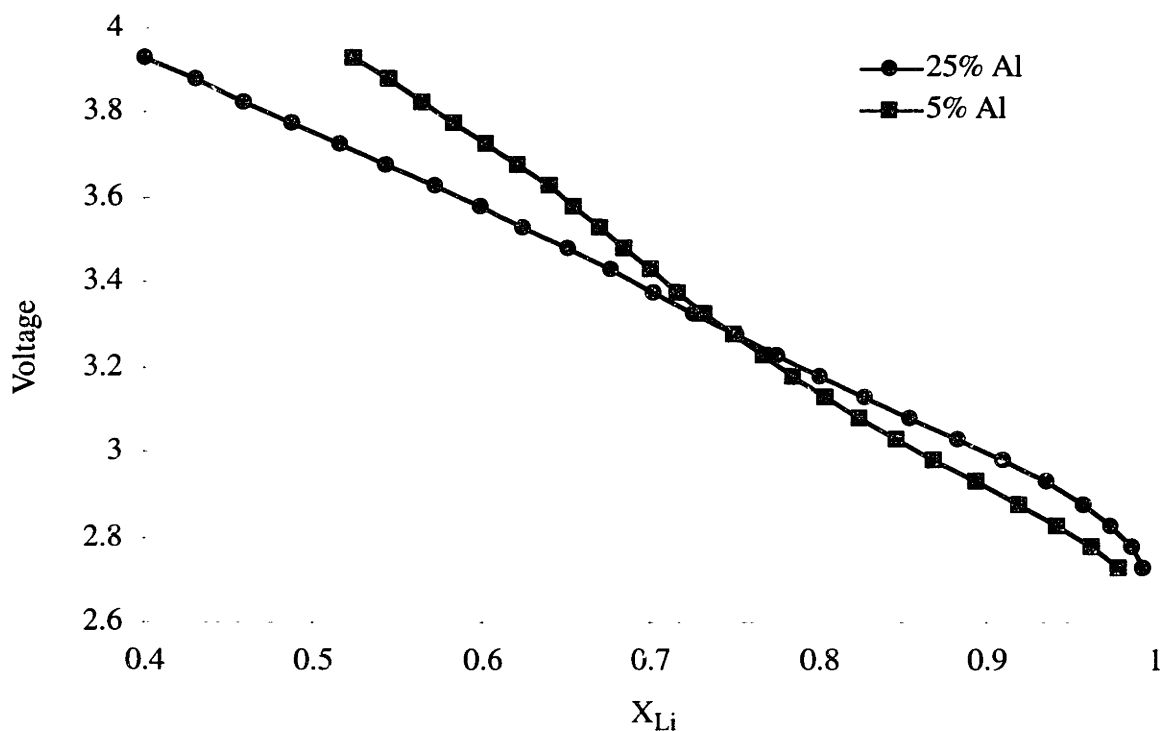c) $Li_{.25}Al_{.25}Co_{.75}O_2$, with 3 vacancies and 1 Li ion (13 ions total).

Figure 4.11: Initial lowering of the intercalation curves as Al content increases.

direct comparison between experiment and calculation is not possible due to the experimentally observed metal-insulator transition in Li_xCoO_2 which keeps the intercalation curve flat at the beginning of charge [40, 72].

The results indicate a subtle interplay between chemical and relaxation effects in determining the site potential for Li ions. It is found that upon charging of $Li_xAl_yCo_{1-y}O_2$ Li first leaves the sites surrounded by one and two Al ions, and subsequently leaves sites surrounded by six Co ions. It is believed that this is due to the size difference between Co^{3+} and Al^{3+} (even though it is small) which causes unfavorable strain in the Li site. The results already give clear indication that simple averaging of the electrochemical potential for mixed-metal systems is not accurate.

4.3.2 Effect of Clustering on Step

The effect of the Al-Co distribution in the system on the shape of the intercalation curve between $x = 0$ and $x = 1$ was also investigated. For $Li_xAl_yCo_{1-y}O_2$ one might expect an abrupt increase in potential for $x < y$. This can be easily rationalized: As Li ions leave the material, Co^{3+} is first oxidized to Co^{4+}. Once all the Co^{3+} is oxidized, further oxidation would require electron extraction from oxygen ions (Al^{3+} is obviously never further oxidized, as it would then be removing an electron from the full 2p shell). However, the Li ions' nearest neighbors are oxygen ions, not Co or Al. If the O ion layers distribute the charge compensation from Li ion removal between all the metal neighbors, a truly homogenous material would have no step in the intercalation voltage curve, only a constant slope. This even slope is what is found on the basis of the first-principles calculations, as shown in Figure 4.12a for a homogeneous mixture of Co and Al ions.

Figure 4.12b shows the intercalation curve with small nanosized Al clustering for 25% Al. Regions of 8 x 8 x 7 Al atoms are sitting in a Co matrix. These small regions of pure Al, approximately two nanometers in size, provide enough sites that are surrounded by only a single metal that the material behaves essentially as a phase separated material. When the Li is removed from the material, it begins by leaving sites within the pure Co matrix. Once these sites are fully vacated, the Li ions leave edge sites where they are surrounded by half Co and
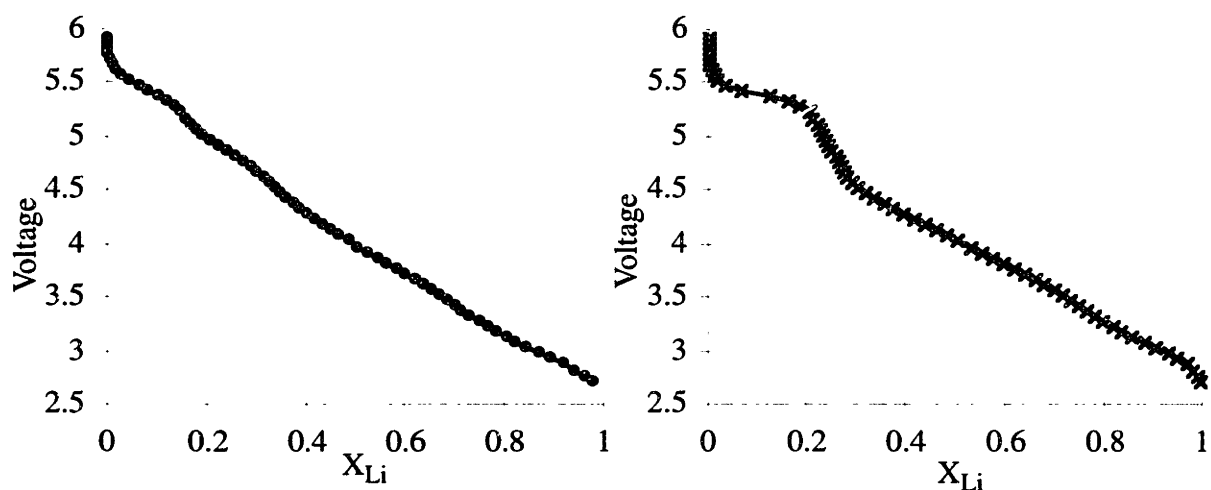
Figure 4.12:   Intercalation curves for $Li_xAl_{0.25}Co_{0.75}O_2$ (a) in a random solid solution, (b) with microsegregated Al regions.

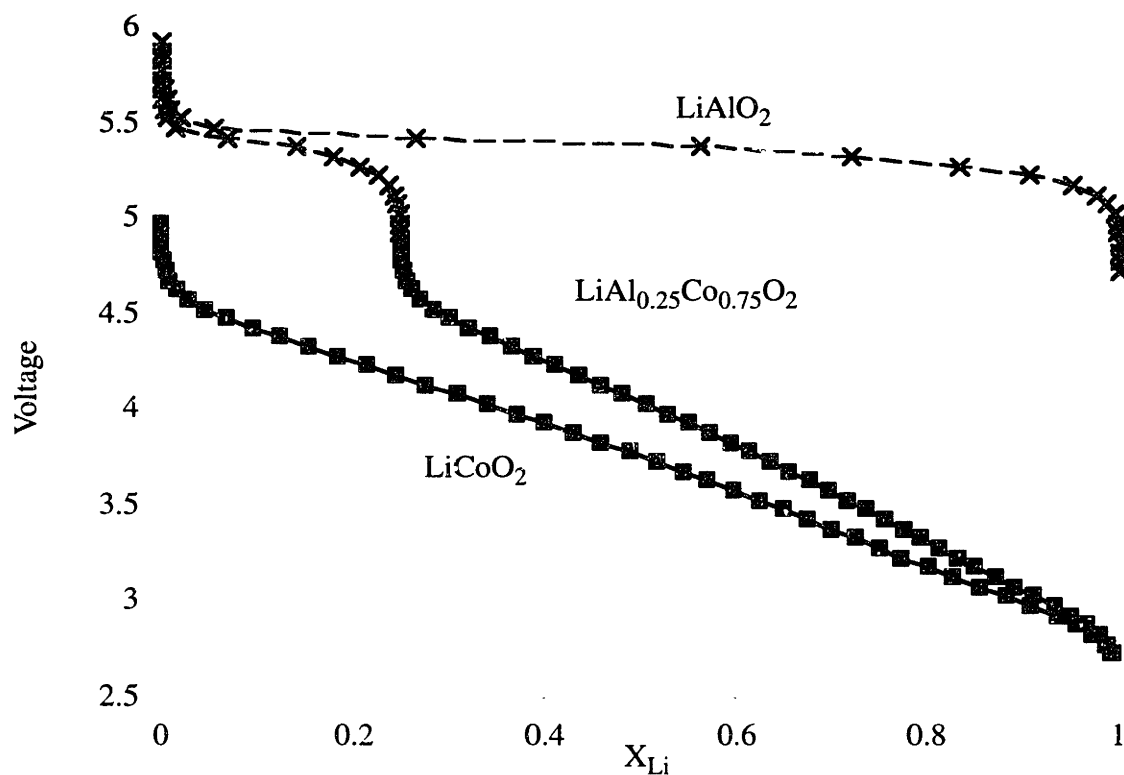Figure 4.13:   Calculated voltage curves for $LiCoO_2$, $LiAlO_2$, and phase separated $LiAl_{0.25}Co_{0.75}O_2$ found by combining the two pure curves.

half Al, and at the end of charging, the last remaining Li ions leave the regions of pure Al. A phase separated material will exhibit a discrete step in the intercalation curve as is often encountered experimentally, similar to Figure 4.12b. First, one type of material is oxidized, then the other. The step shows behavior similar to the result of combining the two pure materials in proportion to the composition, as shown in Figure 4.13.

The results for homogeneous $Li_xAl_yCo_{1-y}O_2$ near the end of charging are more difficult to explain. While common chemistry arguments predict a step in the intercalation curve for $x = y$, the first-principles results only show such step when Al is micro-phase segregated. It is obviously possible that the first-principles methods used in this work to calculate energies fails in the regime near $x = y$. We used a mean field theory for electrons that only includes electron correlation in an approximate way through the exchange-correlation term. The transition from Co^{3+}/Co^{4+} oxidation to oxygen oxidation at $x = y$ may cause substantial electron correlation effects and involve the evolution through a regime with reduced electron conductivity at $x = y$. For x slightly higher than y, the electronic state of the system would consist of a few localized electrons on Co ions (forming Co^{3+}), while for x slightly smaller than y, strong localization of oxygen holes would occur. Such effects would not be captured by the first-principles calculations used here (see Chapter 2 for more details).

4.4 Conclusions

The voltage results for doped spinels calculated in this chapter demonstrate that doping Mn-based spinels with transition metals $(LiM_yMn_{2-y}O_4)$ increases the average Li intercalation voltage without decreasing theoretical capacity. Adding each of the five transition metals studied (M = Cr, Fe, Co, Ni and Cu) to Mn spinel formed new calculated voltage plateaus at potentials 0.25 V (Cr) to 0.78 V (Co) higher than the experimental pure Mn spinel plateau of 4.1 V. The calculated average voltages were less than the experimental results for all dopants except Cu, and three of the five doped voltages were within 0.2 eV. (Co, Ni and Cu). The voltage level of the lower plateau was lower than experimental results as well.

The results indicate that while *on average* the intercalation potential moves upward with Al doping in agreement with previous theoretical [9] and experimental results [56], parts of

the intercalation curve can actually move to a lower potential, indicating a breakdown of simple averaging mixing rules.

Several steps are needed to clarify this issue. A computational study should focus on a system in which the two oxidation steps are at low enough voltage so that they can be accessed reversibly without ambiguity of the process taking place. This should be complemented with a detailed experimental characterization of the structure and transport properties of the material near such a step. In particular, characterization methods that can better capture the short-range local structure, such as NMR or neutron diffraction, would well supplement the XRD data available. For $Li(Ni,Co)O_2$ one such experiment [73] has already indicated tnat short-range clustering actually takes place.

Chapter 5

Effect of Oxygen Defects on the $Li(Al,Co)O_2$ Phase Diagram

All the calculations reported so far have been performed assuming stoichiometric oxygen content. Experiments have shown, however, that layered oxides can form oxygen vacancies during processing and intercalation at elevated temperatures, notably in Li_xNiO_2 and in Li_xCoO_2 (x<1) [74]. The experimental study found that for both the Co and Ni based oxides, the higher the Li content, the greater the temperature needed to promote oxygen liberation. Though these oxygen defects were not found in the fully lithiated compounds at the temperatures tested, the trends indicate that oxygen vacancies might form for fully lithiated $LiCoO_2$ at high enough temperatures. These oxygen vacancies can also alter the $Li(Al,Co)O_2$ phase diagram described in Chapter 3.

The tendency to form oxygen defects can pose a safety hazard. As temperatures rise, these layered lithium oxides can begin to release oxygen gas, building up pressure within the battery. If the internal pressure reaches critical values and the temperature in the material is high enough, the oxygen vents violently, exploding and catching on fire. Thus the tendency of these materials to release oxygen and form vacancies will play a role in creating an ideal lithium battery cathode material.

5.1   Energies of Oxygen Defects

To determine the effect of oxygen defects on the $Li(Al,Co)O_2$ phase diagram, we need to calculate the energy of these defects and relate these to the free energies of the components of

the phase diagram. The stoichiometric phase diagram for $Li(Al,Co)O_2$ is derived and explained in detail in Section 3.3. There are two stable structures for $LiAlO_2$, depending on temperature. Above 600°C, the tetragonal form of $LiAlO_2$ (γ-$LiAlO_2$) is stable. Below 600°C, α-$LiAlO_2$ is stable in the layered α-$NaFeO_2$ structure, space group $R\bar{3}m$. $LiCoO_2$ is stable in the layered α-$NaFeO_2$ structure over all temperature ranges. To incorporate the effect of oxygen vacancies into the phase diagram, we need to calculate the energy of an oxygen defect for all three structures, γ-$LiAlO_2$, α-$LiAlO_2$ and $LiCoO_2$. The total energies of the three structures with both stoichiometric oxygen content and with an oxygen vacancy were calculated using VASP (see Chapter 2 for more details). By comparing the energies of structures with and without an oxygen vacancy, we determined the energy of the oxygen defect. The total cohesive energies and the defect energies are shown in Table 5.1.

	Atoms in Defect Unit Cell	Stoichiometric Energy	Total Energy with Defect	Defect Energy
α-$LiAlO_2$ (layered)	15	-116.459	-103.844	12.62
α-$LiAlO_2$ (layered)	23	-174.689	-162.067	12.62
α-$LiAlO_2$ (layered)	35	-262.033	-249.412	12.62
γ-$LiAlO_2$ (tetragonal)	15	-115.800	-103.792	12.01
$LiCoO_2$ (layered)	35	-251.762	-242.846	8.92

Table 5.1: Stoichiometric and defect energies in eV per oxygen vacancy in α-$LiAlO_2$, γ-$LiAlO_2$, and $LiCoO_2$.

As shown in the first three rows of Table 5 1, we calculated the defect energy for three different defect compositions in the layered α-$LiAlO_{2-z}$ system, $z = 1/8$, $1/12$, and $1/18$, as a convergence test. All three gave the same results for the defect energy within 10 meV. As a result, we assumed that the size of the supercells used was adequate for these approximations. As can be seen in Table 5.1, the oxygen vacancy defect energies are much larger for α-$LiAlO_2$ and γ-$LiAlO_2$ than for $LiCoO_2$. The smaller energy for the Co based material implies that under the same conditions, $LiCoO_2$ will have a greater tendency to form oxygen vacancies

than the Al-based compounds, and thus will be more likely to release oxygen.

5.2   Thermodynamics of Oxygen Defects

In order to incorporate the defect energies into the calculated $Li(Al,Co)O_2$ phase diagram we need to calculate the effect of these defects on the free energy of the layered and tetragonal materials. The chemical potential of oxygen both within the solid and the gas determine the concentration of oxygen vacancies and the change in free energy of the material. To calculate these chemical potentials, an ideal gas model was assumed for the behavior of the oxygen gas. Based on our defect energy calculations and the ideal gas model, we are able to determine the effect of oxygen vacancies on the phase diagram at different temperatures and pressures.

First we related the free energy difference of the structures with and without the defects to the concentration of oxygen vacancies in the non-stoichiometric compound:

$$G_{ns} - G_{st} = G(n_o^{ns}) - G(n_o^{st}) = \int_{n_o^{st}}^{n_o^{ns}} \left(\frac{\partial G}{\partial n_o}\right)_{T, P, N} dn_o \qquad 5.1$$

where G_{ns} is the free energy in the non-stoichiometric solid, G_{st} is the free energy in the stoichiometric solid, n_o^{ns} is the concentration of oxygen in the non-stoichiometric solid, n_o^{st} is the concentration of oxygen in the stoichiometric solid ($n_o^{st} = 1$), T is temperature, P is pressure, and N is total number of particles other than oxygen in the system. The chemical potential of oxygen within the solid can be taken as the derivative of the free energy at constant temperature, pressure, and particles other than oxygen.

$$\mu_o^s = \left(\frac{\partial G}{\partial n_o}\right)_{T, P, N} \qquad 5.2$$

where μ_o^s is the chemical potential of oxygen in the solid.

Next we break the free energy into two parts, separating the configurational entropy contribution from the rest of the free energy:

$$G = G_1 - T \cdot S_c \qquad 5.3$$

where S_c is the configurational entropy and G_1 is the remainder of the free energy. Taking the derivative of the free energy results in two parts of the chemical potential:

$$\frac{\partial G}{\partial n_o} = \frac{\partial}{\partial n_o}(G_1 - T \cdot S_c) = \mu_{1o}{}^s - T \cdot \frac{\partial S_c}{\partial n_o} \qquad 5.4$$

The chemical potential, $\mu_{1o}{}^s$, is assumed to be independent of oxygen concentration, n_o. In this approximation, the dependence of the oxygen chemical potential on concentration is encompassed within the configurational entropy dependent term. Integrating the derivative of free energy from the stoichiometric to the non-stoichiometric composition allows us to find the difference in free energy at different oxygen contents as a function of temperature, oxygen concentration in the non-stoichiometric compound, and the non-configuration part of the chemical potential:

$$G_{ns} - G_{st} = \int_{n_o{}^{st}}^{n_o{}^{ns}} \left(\mu_{1o}{}^s - T \cdot \frac{\partial S_c}{\partial n_o} \right) dn_o \qquad 5.5$$

$$G_{ns} - G_{st} = \mu_{1o}{}^s \cdot [n_o{}^{ns} - 1] - T \cdot S_c(n_o{}^{ns}) \qquad 5.6$$

Both the concentration of oxygen in the non-stoichiometric oxide, $n_o{}^{ns}$, and the non-configurational part of the chemical potential, $\mu_{1o}{}^s$, are needed to determine the free energy change. We can find the concentration of oxygen vacancies as a function of temperature and pressure by relating the chemical potential of oxygen in the solid and the gas. At equilibrium the chemical potential in the solid and in the gas must the same:

$$\mu_o{}^s(n_o{}^{ns}) = \mu_o{}^g(P_o) \qquad 5.7$$

where P_o is the partial pressure of oxygen in the gas. Using Equation 5.4, the chemical potential in the solid can be expressed as:

$$\mu_o{}^s = \mu_{1o}{}^s - T \cdot \frac{\partial S_c}{\partial n_o} \qquad 5.8$$

Assuming the oxygen and vacancies form an ideal solution, the entropy can be written as:

$$S_c = -k_B \cdot [(n_o \cdot \ln(n_o)) + (1-n_o) \cdot \ln(1-n_o)] \qquad 5.9$$

Combining Equations 5.7, 5.8, and 5.9 we can solve for n_o^{ns} to obtain:

$$n_o^{ns} = \frac{1}{1 + \exp\left(\dfrac{1}{k_B T}(\mu_{1o}^s - \mu_o^g(P_o))\right)} \qquad 5.10$$

where is k_B is Boltzmann's constant. Combining Equations 5.10 and 5.6 gives the free energy difference between the stoichiometric and nonstoichiometric oxide as a function of μ_{1o}^s and the chemical potential in the gas, μ_o^g.

By defining the pseudopotential free atom as the standard state for oxygen, the chemical potential of oxygen in the solid, μ_{1o}^s, is the same as the defect energy for the reaction:

$$nLiMO_2 \rightarrow Li_n M_n O_{2n-1} + O \qquad 5.11$$

The total energy change for the reaction is:

$$\Delta E = E(Li_n M_n O_{2n-1}) - n \cdot E(LiMO_{2n}) - E(O) \qquad 5.12$$

The defect energy (E_{defect}), and thus the chemical potential of oxygen in the solid, can be found from the change in cohesive supercell energy:

$$\mu_{1o}^s = E_{defect} = E(Li_n M_n O_{2n-1}) - n \cdot E(LiMO_2) \qquad 5.13$$

The calculated results for the defect energies in $LiCoO_2$, layered α-$LiAlO_2$, and tetragonal γ-$LiAlO_2$, based on the spin-polarized oxygen pseudoatom are:

$$\mu_{1o}^s(Co) = -7.42\,eV$$

$$\mu_{1o}^s(\alpha-Al) = -11.13\,eV \qquad 5.14$$

$$\mu_{1o}^s(\gamma-Al) = -10.52\,eV$$

The chemical potential of an oxygen atom in the gas, $\mu_O{}^g$, relative to the standard state we have defined for oxygen, the pseudopotential free atom, is half the free energy of each molecule with respect to a single atom:

$$\mu_O{}^g = \frac{1}{2} F_{O_2}(T)$$

5.15

Using an ideal gas theory, we can get an approximate value for the free energy of the gas. We calculated the binding energy of oxygen and found it to be:

$$E_{O_2}(T = 0) - 2E_O = -5.71 \text{ eV}$$

5.16

where E_{O_2} is the total energy of an oxygen molecule, and E_O is the total energy of an oxygen atom. Thus we can determine the free energy of the oxygen molecule as a function of temperature and pressure. In this situation, we are considering only the translational and kinetic energy contributions to the energy. Though they may not cancel out entirely, because we are ignoring the viorational effects on the energy of the solid, we also ignore them in the gas. We can therefore use the monatomic ideal gas formula instead of the diatomic because the monatomic formula ignores the vibrational and rotational components of the energy - the same contributions that we are neglecting in the solid. From Callen [76] we have the free energy of a monatomic, non-interacting ideal gas:

$$F_{O_2}(T) = -k_B T \left[\ln \left(\frac{k_B T}{P} \left[\frac{2\pi m_{O_2} k_B T}{h^2} \right]^{\frac{3}{2}} \right) + 1 \right]$$

5.17

where m_{O_2} is the mass of an oxygen molecule and h is Planck's constant. F_{O_2} is the free energy of the gas with respect to E_{O_2}, the energy at zero K. The free energy of the gas with respect to a single oxygen atom can be related to the free energy of the gas with respect to the oxygen molecule:

$$F_{O_2}(T)\{\text{w.r.t } E_O\} = F_{O_2}(T)\{\text{w.r.t } E_{O_2}\} + E_{O_2} - 2E_O(\text{free atom})$$

5.18

Combining Equations 5.15 and 5.18 gives the chemical potential of gaseous oxygen as a

function of temperature and pressure:

$$2\mu_O{}^g = -5.22eV - k_B T \left[\ln\left(\frac{k_B T}{P}\left[\frac{2\pi m_{O_2} k_B T}{h^2} \right]^{\frac{3}{2}} \right) + 1 \right]$$

5.19

Solving Equation 5.19 at 1000 K and air pressure (P_{O_2} = 0.2 atm) gives a value of the chemical potential of:

$$\mu_O{}^g \approx -3.7 eV$$

5.20

Separating temperature from the rest of the factors in Equation 5.19 gives the dependence of the chemical potential on temperature.

$$\mu_O{}^g \approx -5.22eV - k_B T \left[\frac{5}{2}\ln(T) + C \right]$$

5.21

where

$$C = \ln\left(\frac{k_B}{P}\left[\frac{2\pi m_{O_2} k_B}{h^2} \right]^{\frac{3}{2}} \right) + 1$$

5.22

5.3   Effect on Li(Al,Co)O₂ Phase Diagram

With Equations 5.6, 5.9, 5.10, and 5.14 above, the change in free energy was calculated and used to determine the free energy of the non-stoichiometric phase. A new entropy difference, $\Delta S_{\gamma-\alpha}(n_o^{ns})$, was also calculated to ensure that the phase transition remained at 600°C. For the layered phases, the chemical potential of oxygen in the solid, $\mu_O{}^s$, was determined as a function of the temperature and the calculated defect energy for $LiCoO_2$ and $LiAlO_2$ (see Equation 5.8). For intermediate Al concentrations $\mu_O{}^s$ was linearly interpolated between $\mu_O{}^s$ for $LiCoO_2$ and $\mu_O{}^s$ for $LiAlO_2$. This adjusted oxygen chemical potential in the solid state was then used to determine the oxygen concentration, the energy difference, and

67
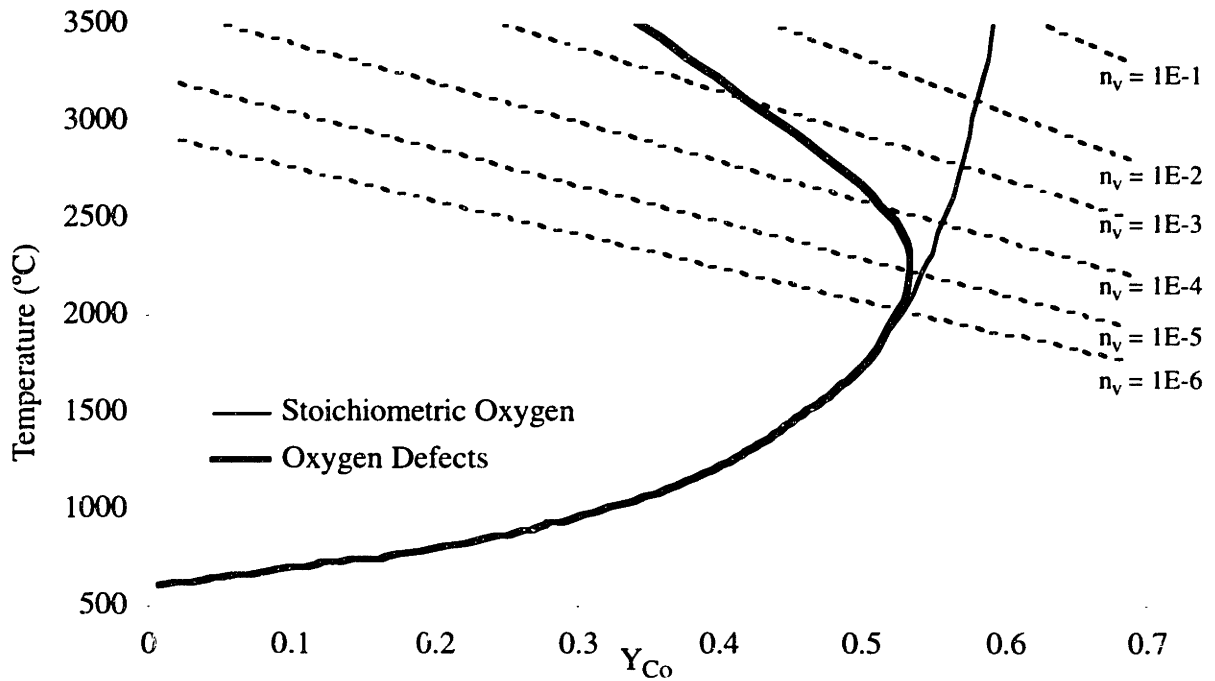
Figure 5.1:   Effect of oxygen vacancies on $LiAl_{1-y}Co_yO_2$ phase diagram. Dashed lines are lines of constant oxygen vacancy concentration, c_v.
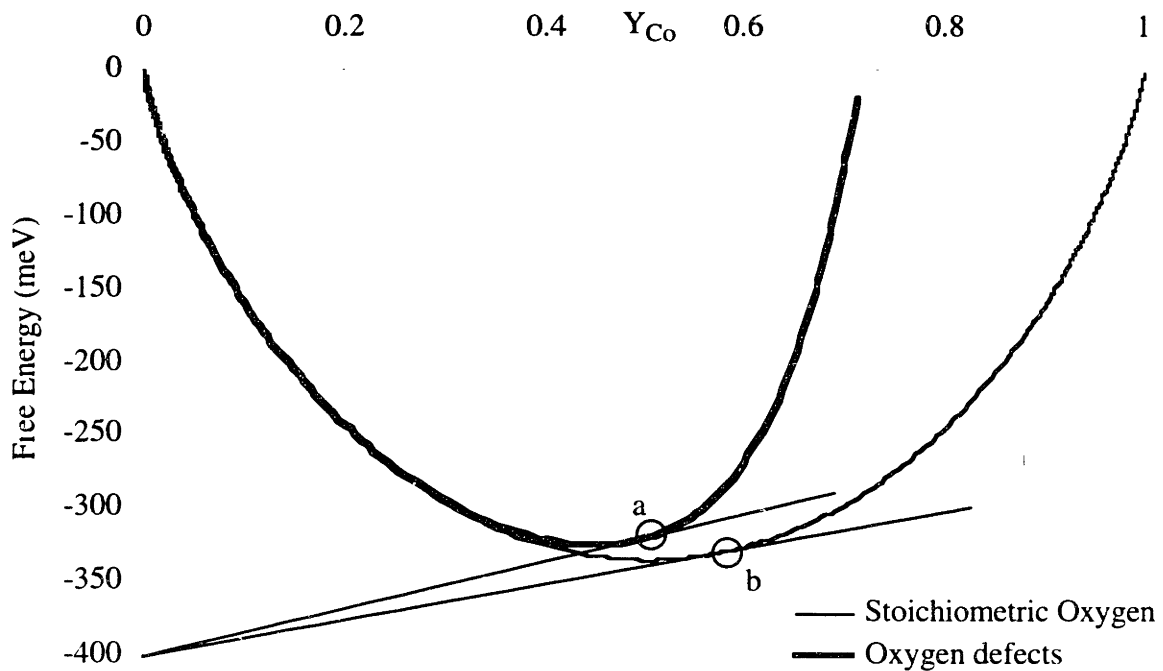

Figure 5.2:   Effect of oxygen vacancies on free energy of layered $LiAl_{1-y}Co_yO_2$ at 3000K. Composition a is the edge of the two-phase region when including the effect of oxygen vacancies, composition b is with stoichiometric oxygen.

the final free energy. From these new free energies, a new phase diagram was calculated, Figure 5.1. For details on finding the phase diagram curves from the free energy, see Section 3.3.

Including the effect of oxygen vacancies in the chemical potential of oxygen (calculated using Equation 5.20) decreased the size of the two phase-region at high temperatures, but showed no change in the phase diagram below 1500°C. The adjustments to the phase diagram are shown in Figure 5.1. Not only does the two-phase region decrease in size due to including oxygen defects, the edge curves backwards towards the $LiAlO_2$ axis. We can see from the defect energies for the different materials (see Table 5.1) that $LiCoO_2$ is much more apt to produce oxygen defects, which will decrease the energy of the Co structure and stabilize the layered compound. This is shown clearly in the lines of iso-concentration plotted in Figure 5.1. The concentration of oxygen vacancies, ($c_v = 1 - n_o^{ns}$) increases with increasing temperature and with increasing cobalt concentration. As the oxygen defect concentration increases, layered $Li(Al,Co)O_2$ becomes more stable and the two-phase region shrinks.

5.4 Discussion

Initially, we anticipated that the adjustment to the phase diagram would bring the calculated phase diagram closer to the experiments described in Section 3.3.3. Because the addition of oxygen defects increases the free energy curves, we expected that the extent of the two-phase region would increase with oxygen vacancies. However, this is not the case. As illustrated in the free energy diagrams at 3000 K, Figure 5.2, the inclusion of oxygen defects does indeed raise the energy, but its raises the energy more towards the Co-rich side – here the number of oxygen defects is greater and thus the change in free energy is more pronounced.

Because the defect energy differs for the two end members, the inclusion of oxygen vacancies changes the free energy of the layered structures non-uniformly. Although the free energy changes for the layered structure are quite small, the effect is much larger on the Co-rich side. This increase in the free energies pushes the edge of the two phase region closer to $LiAlO_2$. Tangent lines are added on the free energy diagram, Figure 5.2, to clarify this effect. At this temperature, the free energy of the $LiAlO_2$ tetragonal phase with respect to the

layered phase is about -400 meV. For the material with oxygen defects, the tangent line intersects the layered free energy curve at concentration a, while for the stoichiometric compound, it crosses at point b. Thus the two-phase region decreases in size with the inclusion of oxygen defects. However, the changes in the phase diagram occur only at high temperatures.

Many approximations have been made in the above method:

- Calibrating the oxygen defect energies with respect to gaseous oxygen is quite approximate. The value obtained experimentally for the binding energy of an oxygen dimer is -5.22 eV, from Huber and Herzberg [75]. Though this is fairly close to the value we obtained using first-principles calculations (-5.71 eV), it is not the same. We also had to adjust the calculated defect energies from the value shown in Table 5.1 to the values shown in Equation 5.14 to adjust for the difference in LDA reference states.

- The initial energy calculations with LDA could be incorrect. LDA methods have been used extensively to calculate energies in lithium oxide materials, but the effect of oxygen vacancies has not been as thoroughly investigated. The energies obtained for the structures with oxygen vacancies could be inaccurate which would make the defect energies inaccurate as well. Nevertheless, the difference in defect energy for $LiCoO_2$ and $LiAlO_2$ are so large (3.7 eV) it is unlikely to be due solely to LDA errors.

- Though a set of calculations was performed to ensure that the defect supercells were large enough, the small size of our cells, 15 to 35 atoms, may affect the defect energies obtained.

- The chemical potential of oxygen in the solid was approximated as linear with concentration. This may be quite in accurate.

- We approximated the non-configurational part of the solid chemical potential as independent of temperature and equal to the calculated energy difference from first principles.

- The assumption that the chemical potential of oxygen in the gas phase has an ideal gas model temperature dependence could be incorrect.

• We neglected rotational and vibrational degrees of freedom for the oxygen gas.

Though many assumptions were made, these preliminary results show the qualitative dependence of the phase diagram on oxygen defects.

$LiNiO_2$ as a cathode material has been shown to have many problems with releasing oxygen. The delithiated Ni and Co materials release much more oxygen than the lithiated structures. To compare the magnitude of the effects of oxygen vacancies, the defect energies were also calculated in $LiNiO_2$, NiO_2, CoO_2, and MnO_2, all in the same layered α-$NaFeO_2$ structure. These results are shown in Table 5.2. For the Co and Ni oxides, the delithiated structures have lower defect energies, and therefore would be more apt to release oxygen. The Ni based materials have lower energies than Co-based oxides or MnO_2. Both of these lower defect energies confirm the experimental results that Li_xNiO_2 releases oxygen more readily than Li_xCoO_2 and MnO_2 and that oxygen is more readily released at lower Li concentrations [74].

	Atoms in Defect Unit Cell	Stoichiometric Energy	Total Energy with Defect	Defect Energy
$LiNiO_2$ (layered)	15	-101.904	running	running
NiO_2 (layered)	26	-180.864	-173.541	7.32
$LiCoO_2$ (layered)	35	-251.762	-242.846	8.92
CoO_2 (layered)	26	-199.920	-192.408	7.51
MnO_2 (layered)	26	-235.802	-226.674	9.13

Table 5.2: Stoichiometric and defect energies in eV per oxygen vacancy in $LiNiO_2$, NiO_2, $LiCoO_2$, CoO_2, and MnO_2.

5.5 Conclusions

Our preliminary results show that oxygen defects do not affect the $Li(Al,Co)O_2$ phase diagram at normal processing temperatures. In addition, this method shows promise for modeling oxygen defects. It correctly predicts that Ni-based layered structures are more likely to release oxygen than Co-based ones, and that the delithiated Ni and Co oxides also have a

higher tendency to form oxygen vacancies.

This work has focused on determining the effect of oxygen defects on the equilibrium phase diagram for $Li(Al,Co)O_2$. This effect may not always be what is relevant. The number of oxygen vacancies may be set at the processing temperature and remain "locked in" as the material is cooled. The cations in the material may then equilibrate with these defects, depending on the diffusivities and relative mobilities of oxygen and the metal cations. These effects may be quite different than what we have calculated and should be considered in future work.

Further investigations, both computational and experimental, need to be performed to refine our defect model and to more closely determine the role of oxygen defects in these materials. We need to examine our assumptions and the size of their effect on the defect model. Defect energy calculations should be performed at intermediate Li concentrations, as well as in the doped material, not just the end members ($LiAlO_2$ and $LiCoO_2$ in this case). Perhaps most importantly, we need to ensure that the oxygen energies are calibrated correctly with respect to gaseous oxygen.

A system for which extensive experimental work has been performed should be identified to compare with the results of this defect model. The effect of oxygen removal on the voltage curves of these cathode materials will also be of interest in addition to the phase stability effects investigated here.

Chapter 6

Conclusions

The goal of this work was to understand the properties of mixed-metal intercalation oxides. Using first-principles methods, we have investigated the effect of doping on the mixing, energetic, and voltage properties as well as the phase diagrams of lithium transition-metal oxides for lithium battery cathode materials. The effect of doping on the phase separation tendencies of layered transition-metal oxides was examined and we found that for normal processing temperatures, Al is miscible in layered transition metal oxides ($LiMO_2$) for five of the eight first-row transition metals studied, (M = Cr, Co, Ni, Cu, and Fe). We calculated a temperature-composition phase diagram for both $Li(Al,Co)O_2$ and $Li(Al,Cr)O_2$. Low temperature miscibility gaps are found for both systems. Al-doping is limited above 600°C by the formation of γ-$LiAlO_2$ and at very low temperatures owing to the existence of a miscibility gap. Reduced solubility is expected in the layered phase above 600°C for all oxides which have substantial solubility with $LiAlO_2$ due to the formation of γ-$LiAlO_2$.

We calculated the effect of transition-metal doping on the average voltage properties in Mn-based spinels, $Li_xM_yMn_{2-y}O_4$ (M = Cr, Fe, Co, Ni and Cu) and predicted the large increase in average voltage found experimentally. We performed a detailed analysis on the layered structure $Li(Al,Co)O_2$, studying the energetics of different lithium sites and the effect of short-range clustering on the shape of the voltage curve. We determined that Li sites with one or two Al nearest neighbors are less stable than those surrounded entirely by Co. Though the *average* voltage is raised by Al substitution, the unexpected stability of sites with a few Al nearest neighbors leads to an initial decrease in voltage. For the Al-doped $LiCoO_2$ system, we find a step in the voltage curve only for micro-segregated materials. When the Al and Co ions

are randomly distributed in a solid solution, the voltage curve shows a continuous, gradual slope.

Finally, we investigated the effect of oxygen defects in the $Li(Al,Co)O_2$ system. We created a model for the effect of oxygen vacancies on the free energy of doped layered oxides by combining an ideal gas approximation for the chemical potential of the oxygen gas and first-principles calculations for the defect energy of an oxygen vacancy. Though we find no effect on the phase diagram for $Li(Al,Co)O_2$ under normal processing conditions, the model does confirm experimental results that oxygen defects affect $LiCoO_2$ much more strongly than $LiAlO_2$, and that delithiated CoO_2 releases oxygen more readily than the lithiated material.

6.1   Suggestions for Future Research

Many of the results obtained in this study pave the way for continuing investigations in doping transition-metal oxides. The solid-solution $Li(Al,Co)O_2$ shows no step and so disagrees with experiments, thus the results for the effect of short-range clustering on the voltage need to be clarified. The absence of a step in the voltage curve of Al-doped $LiCoO_2$ should be interpreted cautiously. Direct energy calculations on each side of the Li composition where the step is expected could verify whether this is a correct LDA result or whether this is due to limitations of the cluster expansion. The voltage behavior at lithium compositions near the step can be directly determined from first-principles energy calculations on supercell structures. In addition, we need to examine the ability of LDA to capture the electron behavior in these doped materials. Examining electronic band structures for these materials as the lithium content varies around the metal substitution level can provide insight into the electronic changes that occur with doping. In addition, another computational study should be performed on a system in which the oxidation steps of the end members are at low enough voltage so that they can be fully examined experimentally. These calculations should be complemented with a detailed experimental characterization of the structure and transport properties of the material near the step.

The existence of metal cations sitting tetrahedral sites in the layered structure needs to be more closely examined. We found that at low Li concentrations, structures with Al ions sitting

in tetrahedral sites have a positive, but small, formation energy. Entropy effects might populate these sites at high enough temperatures. A full investigation of the occupancy of tetrahedral sites as a function of temperature and composition might reveal an explanation for the poor cycling performance of $Li(Al,Co)O_2$. There is a possibility that cation migration from octahedral to tetrahedral sites could occur in other layered systems, such as $LiCoO_2$ and $LiNiO_2$ as well.

Our preliminary results show promise for modeling oxygen defects. However, many assumptions were made in forming the framework of this model. Continued work should be performed to determine the effect of these approximations and use this model on systems with more experimental data. For example, partially delithiated compositions are found to release oxygen at lower temperatures than fully lithiated materials for $LiNiO_2$ and $LiCoO_2$ [74]. Expanding our model to encompass varying lithium concentrations could provide clues as to what dopants could best stabilize these oxygen releasing materials. An experimental investigation by Gao *et al.* [77] into doping layered $LiNiO_2$ with Ti and Mg has shown initially positive results for thermal stability. Further investigations, both computational and experimental, need to be done to refine our defect model and determine the influence of oxygen defects in these materials.

Most of the above suggestions follow directly from the work done in these studies. In addition, there are several possibilities for continuing this work in new directions. Much of this work has focused on the voltage behavior of these lithium oxides. In many lithium battery cathode materials, cycling behavior is just as important as voltage behavior. A first-principles investigation into the cycling problems of these intercalation compounds could prove to be very valuable. Our initial investigation into the possible filling of tetrahedral in the layered materials is one example of how to begin. Long-range effects such as metal cations jumping into the lithium plane during cycling could be examined. The effect of doping on changes in lattice parameters during cycling could offer possible suggestions for decreasing physical breakdown in these materials.

The safety of these materials is also very much an issue. The release of oxygen at low lithium concentrations has proved to be quite dangerous. Why some compounds form oxygen

vacancies and other do not is not clearly understood. Examining structures from both ends of the oxygen defect spectrum could provide insight into the different ways that oxygen behaves in these systems. An investigation into the energetics of why oxygen is released from the delithiated materials more readily than lithiated versions could provide clues as to the behavior of other compounds as well. Preliminary results have shown that doping can decrease oxygen release and therefore greatly enhance materials such as $LiNiO_2$ with potentially good material properties for use in a battery. However, the reasons for the improvements seen with doping are unexplained. If we are to predict which materials will have excellent properties for use in batteries, the behavior of oxygen and the creation of oxygen vacancies in these materials needs to be understood.

Clearly the behavior of doped compounds is not simply a combination of the properties of the constituent elements. In order to determine the best candidates for new battery systems, we must understand the underlying changes that occur to the physical, electrical, and magnetic properties as compounds are mixed. Through first-principles investigations, we have begun to examine some of these effects in this work, but there are many possible avenues to venture down in our quest for new battery materials.

Bibliography

[1] R. J. Gummow, A. de Kock, M. M. Thackeray, "Improved Capacity Retention in Rechargeable 4 V Lithium/Lithium-Manganese Oxide (Spinel) Cells", *Solid State Ionics*, **69**, 59 (1994).

[2] Li Guohua, H. Ikuta, T. Uchida, M. Wakihara, "The Spinel Phases $LiM_yMn_{2-y}O_4$ (M = Co, Cr, Ni) as the Cathode for Rechargeable Lithium Batteries", *J. Electrochem. Soc.*, **143**, 178 (1996).

[3] G. Pistoia, A. Antonini, R. Rosati, C. Bellitto, "Effect of Partial Ga^{3+} Substitution for Mn^{3+} in $LiMn_2O_4$ on its Behaviour as a Cathode for Li Cells", *J. Electroanal. Chem.*, **410**, 115 (1996).

[4] R. Bittihn, R. Herr, D. Hoge, "The Swing System, a Nonaqueous Rechargeable Carbon Metal-Oxide Cell", *J. Power Sources*, **43**, 223 (1993).

[5] K. Amine, H. Tukamoto, H. Yasuda, Y. Fujita, "A New Three-Volt Spinel $Li_{1+x}Mn_{1.5}Ni_{0.5}O_4$ for Secondary Lithium Batteries", *J. Electrochem. Soc.*, **143**, 1607 (1996).

[6] J. M. Tarascon, E. Wang, F. K. Shokoohi, W. R. McKinnon, S. Colson, "The Spinel Phase of $LiMn_2O_4$ as a Cathode in Secondary Lithium Cells", *J. Electrochem. Soc.*, **138**, 2859 (1991).

[7] Q. Zhong, A. Bonakdarpour, M. Zhang, Y. Gao, J. R. Dahn, "Synthesis and Electrochemistry of $LiNi_xMn_{2-x}O_4$", *J. Electrochem. Soc.*, **144**, 205 (1997).

[8] C. Sigala, D. Guyomard, A. Verbaere, Y. Piffard, M. Tournoux, "Positive Electrode Materials with High Operating Voltage for Lithium Batteries: $LiCr_yMn_{2-y}O_4$ ($0 \leq y \leq 1$)", *Solid State Ionics*, **81**, 167 (1995).

[9] G. Ceder, Y.-M. Chiang, D. R. Sadoway, M. K. Aydinol, Y.-I. Jang, B. Huang, "Identification of Cathode Materials for Lithium Batteries Guided by First-Principles Calculations", *Nature*, **392**, 694 (1998).

[10] Y.-M. Chiang, D. R. Sadoway, Y.-I. Jang, B. Huang, H. Wang, "High Capacity, Temperature-Stable Lithium Aluminum Manganese Oxide Cathodes for Rechargeable Batteries", *Electrochem. Solid-State Lett.*, **2**, 107 (1999).

[11] T. Ohzuku, T. Yanagawa, M. Kouguchi, A. Ueda, "Innovative Insertion Material of $LiAl_{1/4}Ni_{3/4}O_2$ ($R\bar{3}m$) for Lithium-Ion (Shuttlecock) Batteries", *J. Power Sources*, **68**, 131 (1997).

[12] A. F. Kohan, *Total-Energy Models for Phase-Stability Studies in Multicomponent Oxides*, PhD thesis, Massachusetts Institute of Technology (1997).

[13] P. Hohenberg and W. Kohn, "Inhomogeneous Electron Gas", *Phys. Rev.*, **136**, B864 (1964).

[14] W. Kohn and L. J. Sham, "Self-Consistent Equations Including Exchange and Correlation Effects", *Phys. Rev.*, **140**, A1133 (1965).

[15] G. Ceder, M. K. Aydinol, A. F. Kohan, "Application of First-Principles Calculations to the Design of Rechargeable Li-Batteries", *Comput. Mater. Sci.*, **8**, 161 (1997).

[16] W. Zhong, D. Vanderbilt, K. M. Rabe, "First-Principles Theory of Ferroelectric Phase-Transitions for Perovskites - the Case of $BaTiO_3$", *Phys. Rev. B*, **52**, 6301 (1995).

[17] M. C. Payne, M. P. Teter, D. C. Allan, T. A. Arias, J. D. Joannopoulos, "Iterative Minimization Techniques for Ab Initio Total-Energy Calculations - Molecular Dynamics and Conjugate Gradients", *Rev. Mod. Phys.*, **64**, 1045 (1992).

[18] K. M. Glassford and J. R. Chelikowsky, "Structural and Electronic-Properties of Titanium Dioxide", *Phys. Rev. B*, **46**, 1284 (1992).

[19] M. J. Gillan, I. Manassidis, A. De Vita, "The Ab-Initio Energetics of Oxides", *Philos. Mag. B*, **69**, 879 (1994).

[20] Y. Bar-Yam, S. T. Pantelides, J. D. Joannopoulos, "Ab-Initio Pseudopotential Solid-State Calculations of Highly Electronegative 1st-row Elements", *Phys. Rev. B*, **39**, 3396 (1989).

[21] A. F. Kohan and G. Ceder, "Tight-Binding Calculation of Formation Energies in Multicomponent Oxides: Application to the MgO-CaO Phase Diagram", *Phys. Rev. B*, **54**, 805 (1996).

[22] M. K. Aydinol, A. F. Kohan, G. Ceder, K. Cho, J. Joannopoulos, "Ab Initio Study of Lithium Intercalation in Metal Oxides and Metal Dichalcogenides", *Phys. Rev. B*, **56**, 1354 (1997).

[23] G. Kresse, J. Furthmüller, "Efficient Iterative Schemes for Ab Initio Total-Energy Calculations Using a Plane-Wave Basis Set", *Phys. Rev. B*, **54**, 11169 (1996).

[24] G. Kresse, J. Furthmüller, "Efficiency of Ab-Initio Total Energy Calculations for Metals and Semiconductors Using a Plane-Wave Basis Set", *Comput. Mater. Sci.*, **6**, 15 (1996).

[25] G. Kresse, J. Hafner, "Ab-Initio Molecular-Dynamics Simulation of the Liquid-Metal Amorphous-Semiconductor Transition in Germanium", *Phys. Rev. B*, **49**, 14251 (1994).

[26] D. Vanderbilt, "Soft Self-Consistent Pseudopotentials in a Generalized Eigenvalue Formalism", *Phys. Rev. B*, **41**, 7892 (1990).

[27] D. M. Ceperley and B. J. Alder, "Ground State of the Electron Gas by a Stochastic Method", *Phys. Rev. Lett.*, **45**, 566 (1980).

[28] J. P. Perdew and A. Zunger, "Self-Interaction Correction to Density-Functional Approximations for Many-Electron Systems", *Phys. Rev. B*, **23**, 5048 (1981).

[29] H. J. Monkhorst and J. D. Pack, "Special Points for Brillouin-Zone Integrations", *Phys. Rev. B*, **13**, 5188 (1976).

[30] M. Methfessel and A. T. Paxton, "High-Precision Sampling for Brillouin-Zone Integration in Metals", *Phys. Rev. B*, **40**, 3616 (1989).

[31] P. E. Blöchl, O. Jepsen, O. K. Andersen, "Improved Tetrahedron Method for Brillouin-Zone Integrations", *Phys. Rev. B*, **49**, 16223 (1994).

[32] M. K. Aydinol and G. Ceder, "First-Principles Prediction of Insertion Potentials in Li-Mn Oxides for Secondary Li Batteries", *J. Electrochem. Soc.*, **144**, 3832 (1997).

[33] G. Ceder and A. Van der Ven, "Phase Diagrams of Lithium Transition Metal Oxides: First Principles Investigations", *Electrochim. Acta, in press*(1999).

[34] J. M. Sanchez, F. Ducastelle, D. Gratias, "Generalized Cluster Description of Multicomponent Systems", *Physica A*, **128**, 334 (1984).

[35] G. Ceder, P. D. Tepesch, A. F. Kohan, A. Van der Ven, "A Model to Predict Ionic Disorder and Phase Diagrams: Application to CaO-MgO, Gd_2O_3-ZrO_2, and to sodium β"-alumina", *J. Electroceram.*, **1**, 15 (1997).

[36] G. Ceder, "Phase Diagrams: Ab Initio Computation", In *Encyclopedia of Advanced Materials*, D. Bloor, R. J. Brook, M. C. Flemings, S. Mahajan, Editors, 1951, Pergamon Press, Oxford (1994).

[37] D. de Fontaine, "Cluster Approach to Order-Disorder Transformations in Alloys", In *Solid State Physics*, H. Ehrenreich, D. Turnbull, Editors, **47**, 33, Academic Press (1994).

[38] G. Ceder, "A Derivation of the Ising Model for the Computation of Phase Diagrams", *Comput. Mater. Sci.*, **1**, 144 (1993).

[39] D. de Fontaine, "Configurational Thermodynamics of Solid Solutions", In *Solid State Physics*, H. Ehrenreich, F. Seitz, D. Turnbull, Editors, **34**, 73, Academic Press (1979).

[40] A. Van der Ven, M. K. Aydinol, G. Ceder, G. Kresse, J. Hafner, "First-Principles Investigation of Phase Stability in Li_xCoO_2", *Phys. Rev. B*, **58**, 2975 (1998).

[41] A. Van der Ven, G. Ceder, "Electrochemical Properties of Spinel Li_xCoO_2: A First-Principles Investigation", *Phys. Rev. B*, **59**, 742 (1999).

[42] P. D. Tepesch, G. D. Garbulsky, G. Ceder, "Model for Configurational Thermodynamics in Ionic Systems", *Phys. Rev. Lett.*, **74**, 2272 (1995).

[43] G. D. Garbulsky, G. Ceder, "Linear-Programming Method for Obtaining Effective Cluster Interactions in Alloys from Total-Energy Calculations - Application to the FCC Pd-V System", *Phys. Rev. B*, **51**, 67 (1995).

79

[44]   A. Zunger, "First-Principles Statistical Mechanics of Semiconductor Alloys and Intermetallic Compounds", in *Statics and Dynamics of Alloy Phase Transformations*, P. E. A. Turchi, A. Gonis, Editors, 361, Plenum Press, New York (1994).

[45]   P. D. Tepesch, A. F. Kohan, G. D. Garbulsky, G. Ceder, C. Coley, H. T. Stokes, L. L. Boyer, M. J. Mehl, B. Burton, K. Cho, J. Joannopoulos, "A Model to Compute Phase Diagrams in Oxides with Empirical or First-Principles Energy Methods and Application to the Solubility Limits in the CaO-MgO System", *J. Am. Ceram. Soc.*, **79**, 2033 (1996).

[46]   K. Mizushima, P. C. Jones, P. J. Wiseman, J. B. Goodenough, "Li_xCoO_2 ($0 < x \leq 1$): A New Cathode Material for Batteries of High Energy Density", *Mater. Res. Bull.*, **15**, 783 (1980).

[47]   K. Mizushima, P. C. Jones, P. J. Wiseman, J. B. Goodenough, "Li_xCoO_2 ($0 < x \leq 1$): A New Cathode Material for Batteries of High Energy Density", *Solid State Ionics*, **3/4**, 171 (1981).

[48]   T. A. Hewston and B. L. Chamberland, "A Survey of First-Row Ternary Oxides $LiMO_2$ (M = Sc - Cu)", *J. Phys. Chem. Solids*, **48**, 97 (1987).

[49]   A. Rougier, C. Delmas, A. V. Chadwick, "Noncooperative Jahn-Teller Effect in $LiNiO_2$ - an EXAFS Study", *Solid State Commun.* **94**, 123 (1995).

[50]   R. D. Shannon, "Revised Effective Radii and Systematic Studies of Interatomic Distances in Halides and Chalcogenides", *Acta Crystallogr.*, **A32**, 751 (1976).

[51]   H.-A. Lehmann and H. Hesselbarth, "Über eine neue Modifikation des $LiAlO_2$", *Z. Anorg. Allg. Chem.*, **313**, 117 (1961).

[52]   M. Marezio and J. P. Remeika, "High Pressure Synthesis and Crystal Structure of α-$LiAlO_2$", *J. Chem. Phys.*, **44**, 3143 (1966).

[53]   T. Ohzuku, A. Ueda, M. Kouguchi, "Synthesis and Characterization of $LiAl_{1/4}Ni_{3/4}O_2$ ($R\bar{3}m$) for Lithium-Ion (Shuttlecock) Batteries", *J. Electrochem. Soc.*, **142**, 4033 (1995).

[54]   G. A. Nazri, A. Rougier, K. F. Kia, "Synthesis, Characterization, and Electrochemical Performances of Substituted Layered Transition Metal Oxides, $LiM_{1-y}M'_yO_2$, (M = Ni and Co, M' = B and Al)", *Mater. Res. Soc. Symp. Proc.*, **453**, 635 (1997).

[55]   R. Alcántara, P. Lavela, P. L. Relaño, J. L. Tirado, E. Zhecheva, R. Stoyanova, "X-ray Diffraction, EPR and Li and Al-MAS NMR Study of $LiAlO_2$-$LiCoO_2$ Solid Solutions", *Inorg. Chem.*, **37**, 264 (1998).

[56]   Y.-I. Jang, B. Huang, H. Wang, D. R. Sadoway, G. Ceder, Y.-M. Chiang, H. Liu, H. Tamura, "$LiAl_yCo_{1-y}O_2$ ($R\bar{3}m$) Intercalation Cathode for Rechargeable Lithium Batteries", *J. Electrochem. Soc.*, **146**, 862 (1998).

[57] Y.-I. Jang, B. Huang, Y.-M. Chiang, D. R. Sadoway, "Stabilization of $LiMnO_2$ in the α-$NaFeO_2$ Structure Type by $LiAlO_2$ Addition", *Electrochem. Solid-State Lett.*, **1**, 13 (1999).

[58] Q. Zhong and U. von Sacken, "Crystal Structures and Electrochemical Properties of $LiAl_yNi_{1-y}O_2$ Solid Solution", *J. Power Sources*, **54**, 221 (1995).

[59] K. R. Poeppelmeier, S. H. Thong, "Solid Solution in the $LiAlO_2$-$LiCrO_2$ Ternary Oxide System", *J. Less-Common Met.*, **156**, 291 (1989).

[60] H. Kawai, M. Nagata, H. Tukamoto, A. R. West, "A Novel Cathode $Li_2CoMn_3O_8$ for Lithium Ion Batteries Operating Over 5 Volts", *J. Mater. Chem.*, **8**, 837 (1998).

[61] T. Ohzuku, A. Ueda, M. Nagayama, Y. Iwakoshi, H. Komori, "Comparative Study of $LiCoO_2$, $LiNi_{1/2}Co_{1/2}O_2$ and $LiNiO_2$ for 4 Volt Secondary Lithium Cells", *Electrochim. Acta*, **38**, 1159 (1993).

[62] H. Kawai, M. Nagata, H. Tukamoto, A. R. West, "A New Lithium Cathode $LiCoMnO_4$: Toward Practical 5 V Lithium Batteries", *Electrochem. Solid-State Lett.*, **1**, 212 (1998).

[63] H. Kawai, M. Nagata, M. Tabuchi, H. Tukamoto, A. R. West, "Novel 5 V Spinel Cathode $Li_2FeMn_3O_8$ for Lithium Ion Batteries", *Chem. Mater.*, **10**, 3266 (1998).

[64] H. Kawai, M. Nagata, H. Kageyama, H. Tukamoto, A. R. West, "5 V Lithium Cathodes Based on Spinel Solid Solutions $Li_2Co_{1+x}Mn_{3-x}O_8$", *Electrochem. Solid-State Lett, in press* (1999).

[65] H. Kawai, M. Tabuchi, M. Nagata, H. Tukamoto, A. R. West, "Crystal Chemistry and Physical Properties of Complex Lithium Spinels $Li_2MM'_3O_8$ (M = Mg, Co, Ni, Zn; M' = Ti, Ge)", *J. Mater. Chem.*, **8**, 1273 (1998).

[66] Y. Ein-Eli, S. H. Lu, W. F. Howard, Jr., S. Mukerjee, J. McBreen, J. T. Vaughey, M. M. Thackeray, "$LiMn_{2-x}Cu_xO_4$ Spinels $0.1 \leq x \leq 0.5$ - A New Class of 5 V Cathode Materials for Li Batteries", *J. Electrochem. Soc.*, **145**, 1238 (1998).

[67] Y. Ein-Eli and W. F. Howard, Jr., "$LiCu^{II}_xCu^{III}_yMn^{III,IV}_{[2-(x+y)]}O_4$: 5 V Cathode Materials", *J. Electrochem. Soc.*, **144**, L205 (1997).

[68] M. N. Obrovac, Y. Gao, J. R. Dahn, "Explanation for the 4.8-V Plateau in $LiCr_xMn_{2-x}O_4$", *Phys. Rev. B*, **57**, 5728 (1998).

[69] D. Song, H. Ikuta, T. Uchida, M. Wakihara, "The Spinel Phases $LiAl_yMn_{2-y}O_4$ (y = 0, 1/12, 1/9, 1/6, 1/3) and $Li(Al,M)_{1/6}Mn_{11/6}O_4$ (M = Cr, Co) as the Cathode for Rechargeable Lithium Batteries", *Solid State Ionics*, **117**, 151 (1999).

[70] P. D. Tepesch, *Atomistic Modeling of Ceramic Materials: Predicting Crystal Structures, Thermodynamic Properties, and Diffusion Behavior*, PhD thesis, Massachusetts Institute of Technology (1996)

[71] M. K. Aydinol, A. Van der Ven, G. Ceder, "Application of Ab Initio Methods to Secondary Lithium Batteries", *Mater. Res. Soc. Symp. Proc.*, **496**, 65 (1998).

[72] M. Menetrier, I. Saadoune, S. Levasseur, C. Delmas, "The Insulator-Metal Transition Upon Lithium Deintercalation for $LiCoO_2$: Electronic Properties and ^7Li NMR Studies", *Chem. Mater.*, *in press* (1999).

[73] M. Menetrier, A. Rougier, C. Delmas, "Cobalt Segregation in the $LiNi_{1-y}Co_yO_2$ Solid-Solution - A Preliminary ^7Li NMR Study", *Solid State Commun.*, **90**, 439 (1994).

[74] J. R. Dahn, E. W. Fuller, M. Obrovac, U. von Sacken, "Thermal Stability of Li_xCoO_2, Li_xNiO_2 and λ-MnO_2 and Consequences for the Safety of Li-Ion Cells", *Solid State Ionics*, **69**, 265 (1994).

[75] K. P. Huber and G. Herzberg, *Molecular Structure and Molecular Spectra. IV. Constants of Diatomic Molecules*, Van Nostrand Reinhold (1979).

[76] H. B. Callen, *Thermodynamics and an Introduction to Thermostatistics, Second Edition*, p 373, John Wiley & Sons, New York (1985).

[77] Y. Gao, M. V. Yakovlea, W. B. Ebner, "Novel $LiNi_{1-x}Ti_{x/2}Mg_{x/2}O_2$ Compounds as Cathode Materials for Safer Lithium-Ion Batteries", *Electrochem. Solid-State Lett.*, **1**, 117 (1998).

THESIS PROCESSING SLIP

FIXED FIELD: ill. _____ name _____

index _____ biblio _____

► COPIES: (Archives) Aero Dewey Eng Hum

Lindgren Music Rotch (Science)

TITLE VARIES: ► ☐ _____

_____

NAME VARIES: ► ☑ ✓ Hume _____

_____

IMPRINT: (COPYRIGHT) _____

► COLLATION: _____ 82 P _____

► ADD: DEGREE: _____ ► DEPT.: _____

SUPERVISORS: _____

_____

_____

_____

_____

_____

_____

_____

_____

NOTES:

	cat'r:	date:
		page:
► DEPT: MatSci & E.	►	

► YEAR: 1999 ► DEGREE: S. M.

► NAME: BUTA, Sarah H.